2017

Investigation of Heat Transfer Enhancement Within a Concentric Annulus

Alexander Hanhold
University of Central Florida

INVESTIGATION OF HEAT TRANSFER ENHANCEMENT WITHIN A CONCENTRIC ANNULUS

by

ALEX HANHOLD
B.S. University of Central Florida, 2014

A thesis submitted in partial fulfillment of the requirements
for the degree of Master of Science
in the Department of Mechanical and Aerospace Engineering
in the College of Engineering and Computer Science
at the University of Central Florida
Orlando, Florida

Fall Term
2017

Major Professor: Jayanta Kapat

ABSTRACT

Effective heat exchange is key for many energy applications including heat exchangers, heat extraction from heat source, and heat rejection to ambient thermal sink. This study focuses on the investigation for a specific heat exchange configuration, namely heat removal within a concentric annular passage using helical turbulators and jet impingement.

Numerical testing was used to see how the different geometric parameters affect the heat transfer and pressure drop within the annulus by using helicoil turbulators. A vast range of designs were studied by changing the turbulator shape, pitch, and blockage ratio while maintaining a constant Reynolds number of 25,000. CFD was performed in STARCCM+ using the realizable κ-ε turbulence model. Results show that turbulence and heat transfer increase with a higher blockage ratio and smaller pitch but the pressure drop is subsequently increased as well. The square turbulator promoted higher heat transfer compared to the circle turbulator but the pressure drop was significantly increased when the helix angle was greater than 20° and blockage ratio greater than 0.48.

Experimental and numerical efforts were used to find the heat transfer due to impingement jets on the target surface. Multiple flows as a function of jet Reynolds number ranging from 16,000-33,000 were tested for two geometries. Temperature Sensitive Paint (TSP) was utilized to observe local heat transfer. It was observed that jet degradation occurs after the 6^{th} row of stream-wise impingement jets for both cases experimentally and it was difficult to numerically capture the effect of the cross flow from previous jets but managed to follow the same trend. The numerical results showed that they can be used with good agreement to predict

the surface averaged Nusselt number to be within the 12% uncertainty found from experimental efforts. Geometry B was determined to perform better in terms of heat transfer as opposed to Geometry A with the same pressure loss.

This paper is dedicated to my family,
including my parents, Jeff and Diana, my brother Eric and my cat Leo.

ACKNOWLEDGMENTS

I would like to acknowledge the support of my advisor, Dr. Jayanta Kapat, as well as the many other members of CATER. Without their useful advice and discussion, the current work would not have been completed.

TABLE OF CONTENTS

LIST OF FIGURES

LIST OF TABLES

CHAPTER 1: INTRODUCTION

Heat exchangers are one of the more important and widely used pieces of equipment that are available today for heat transfer. They are designed to transfer heat from one medium to another by the use of a fluid or gas. These devices are widely used in air conditioning, power generation such as steam and gas turbines, nuclear plants and sewage treatment plants just to name a few. There are a vast number of different types of heat exchangers out there which are geared towards individual or specific areas of interest in terms of heating or cooling a fluid or object. Some of the more common types of heat exchangers are: shell and tube, helical-coil, plate, direct contact and micro channel.

One of the most widely uses of heat exchangers is for air conditioning for buildings and vehicles. For these cases there are typically tubing that is in a serpentine fashion that have some type of liquid coolant flowing through it. With a cross-flow of warmer air coming over those serpentine tubes, a heat exchange will take place cooling down the air for the people and slightly heating up the liquid coolant.

Geothermal heat exchangers are commonly used for houses and building. It is estimated that geothermal systems can save 40%-70% on home heating and 20%-50% on home cooling costs over conventional systems. The drawback is that there is a high cost of installation that can cost up to $12,000 [1].

As heat exchangers continue to develop and improve efficiency in cooling or heating the respective area of concern, the thermal load for these heat exchangers will continue to increase.

For the increase in thermal load there needs to be some sort of heat transfer enhancement that happens within the heat exchanger to accommodate the higher temperatures.

Internal duct cooling is a process in which coolant flows and removes heat from the inside surface of the hot object to prevent melting/failure. This is used extensively in environments that are subjected to a large thermal load such gas turbines where parts experience extremely hot temperatures in order to achieve a higher energy output and thermal efficiency. Some common types of internal duct cooling are dimples (negative features), hemispherical protrusions (positive features, pimples), rib turbulators and pin-fins. These features create local flow separation and reattachment zones as well as promote mixing of the flow to improve the rate at which heat transfer occurs.

The goal of heat enhancement is to reduce the size and cost of heat exchanger equipment, or to increase the heat duty for a given size heat exchanger. This is done by using passive enhancement. This consists of alteration to the heat transfer surface or incorporation of a device whose presence results in a flow field modification.

CHAPTER 2: LITERATURE REVIEW

There has been extensive research on convective heat transfer within an annulus starting in the late 1950's.

Annulus Heat Transfer

Dirker [2] contributed adding correlations for concentric smooth pipe annular flow. The experiments were conducted with a vast range of annular diameter ratios of 1-31. Hot water was run through the center tube and cold water was run through the annulus. The Wilson plot method was used to develop a convective heat transfer correlation for annular diameter ratios of 1.7-3.2 and Reynolds numbers ranging from 4,000 - 30,000. This correlation developed predicted internal and annular Nusselt number values accurately within 3% of experimental results which are shown in Equations 2.1 and 2.2. P, C_i and C_o are added to account for geometry influences with *a* being the annular diameter ratio.

$$Nu_i = \frac{h_i D_h}{k_i} = C_i Re_i^{0.8} Pr_i^{\frac{1}{3}} (\frac{\mu}{\mu_w})_i^{0.14} \quad (2.1)$$

$$Nu_o = \frac{h_o D_h}{k_o} = C_o Re_{o,D_h}^{P} Pr_o^{\frac{1}{3}} (\frac{\mu}{\mu_w})_0^{0.14} \quad (2.2)$$

$$P = 1.013e^{-0.067a} \quad (2.3)$$

$$C_o = \frac{0.003a^{1.86}}{0.063a^3 - 0.674a^2 + 2.225a - 1.157} \quad (2.4)$$

Gnielinski [3] developed a correlation based on a large number of experimental data from literature for heat transfer coefficient for turbulent flow in concentric annular ducts. Gnielinski took Dirker's correlations and extended it by factors that take into consideration the effect of the

diameter ratio of the annulus, how the friction factor is affected by the diameter ratio and the different boundary conditions for heating or cooling. The different boundary conditions investigated are shown in Figure 2.1. Here option a) has heat transfer from the inner tube while the outer tube in insulated. Option b) has the heat transfer from the outer tube and the inner tube insulated and option c) has heat transfer from both tubes to the annular flow.

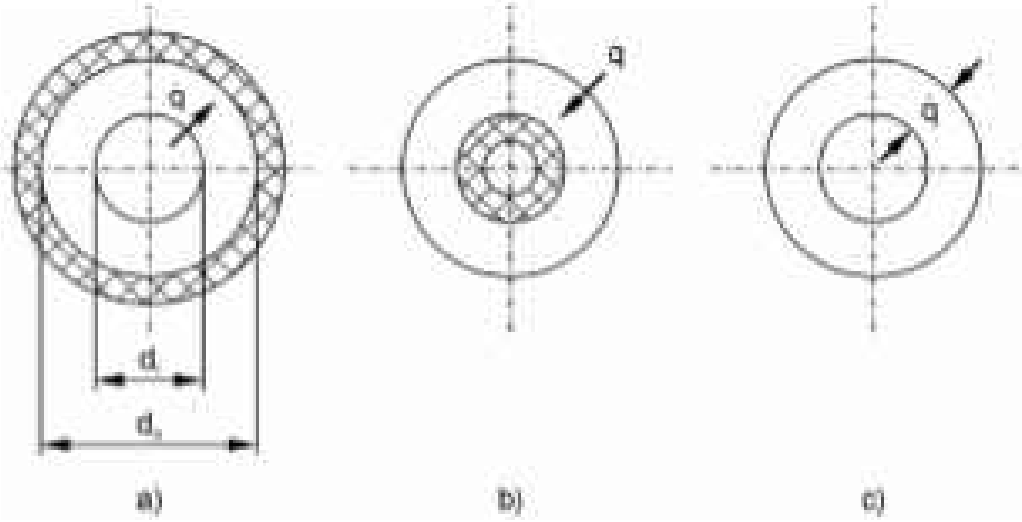

Figure 2.1: Annulus Flow Boundary Conditions

Prandtl [4] created similar correlation for turbulent flow that incorporated friction factor. Prandtl developed Equation 2.5 shown below .

$$Nu = \frac{\left(\frac{f}{8}\right)RePr}{1+8.7\sqrt{\frac{f}{8}}(Pr^n-1)} \tag{2.5}$$

For turbulent flow with a Reynold number greater than 10,000 the correlation for Nusselt number that Gnielinski created is shown in Equation 2.6 where L is the length of the annulus in meters.

$$Nu = \frac{(f_{ann}/8)RePr}{k_1+12.7\sqrt{f_{ann}/8}(Pr^{2/3}-1)}[1 + (\frac{d_h}{L})^{\frac{2}{3}}]F_{ann}K \quad (2.6)$$

$$k_1 = 1.07 + \frac{900}{Re} - \frac{0.63}{(1+10\mathrm{Pr})} \quad (2.7)$$

$$f_{ann} = (1.8\log_{10} Re^* - 1.5)^{-2} \quad (2.8)$$

$$Re^* = Re\frac{(1+a^2)\ln a+(1-a^2)}{(1-a)^2\ln a} \quad (2.9)$$

$$F_{ann} = 0.75a^{-0.17} \quad (2.10)$$

Table 2.1 shows all the different annular diameter ratios as well as the respective Reynolds number ranges that each experiment tested for Gnielinski's correlation.

Table 2.1: Annular Diameter Ratios and Reynolds Numbers Investigated

Author	Year	Boundary Condition	Fluid	Annular Diameter ratio (d_i/d_o)	Reynolds Number
Lee et al.	1964	a	Air	0.258-0.613	10,000-50,000
Quarmby	1967	a	Air	0.1093-0.347	15,000-300,000
Zerban	1940	a	Air	0.518-0.84	10,000-45,000
Dirker et al.	2005	a	Water	0.198-0.595	10,000-35,000
Petukhov et al.	1963	b	Air	0.0718-0.692	10,000-300,000
Koch et al.	1958	b	Air	0.2122-0.838	10,000-50,000
Leung et al.	1962	b	Air	0.192-0.5	10,000-200,000
Krischer	1961	b	Water	0.4-0.816	10,000-22,000

Petukhov et al [5] investigated how turbulent flow through an annulus can affect heat transfer when the inner tube is heated while the outer tube is insulated and vice versa. The measurements were conducted with constant heat flux on the heated surface. The annular diameter ratio ranged from 0.0718-0.692. Local Nusselt numbers were found on the inner and outer pipes for Reynolds ranging from 10,000-300,000.

Kays et al. [6] experimentally investigated turbulent flow in a circular tube annulus. Annular diameter ratio ranged from 0.1-0.8, Reynolds numbers from 10,000 – 100,000 and vast range of Prandtl numbers were determined. A compilation of Nusselt numbers were found for different cases where there was heating from the inner tube or heating from the outer tube.

Heat Transfer Enhancement

Promvonge et al. [7] studied heat transfer in a pipe with conical nozzle turbulators using a uniform heat flux pipe. Pitch ratios of 2, 4 and 7 and a Reynolds number range of 8,000-18,000 were investigated in this paper. It was found that the heat transfer increase was as high as 315%

for a pitch ratio of 2. To conclude, the smallest pitch ratio and smallest Reynolds number performed the best at enhancing heat transfer.

Iacovides et al. [8] numerically investigated heat transfer in two-dimensional passages with ribbed turbulators using low-Re models. These passages included ribbed annular channels, pipes and plane channels. The annular channels had ribs on the inner annulus wall with the annulus maintaining an annular diameter ratio of 0.392 with the rib P/e being 10.8 and 20. The κ-ε model chosen well represented the experimental data showing the recirculation zones caused by the turbulators.

Wang et al. [9] numerically studied the heat transfer and pressure drop performance in an annulus using interrupted wavy, sinusoidal wavy and plain fins on the internal pipe for Reynolds numbers ranging from 904-4,520. The κ-ε model was again chosen due to its good performance in predicting flow separation. It was concluded that the wavy fins produced higher heat transfer but at a cost of increased pressure drop. The numeric results showed that the steady and spatially periodic growth and disruption of cross-sectional vortices occurred near the tube/fin walls along the streamwise locations causing the overall heat transfer coefficients in wavy channels to be higher than those in a straight fin channel. Yu et al. [10] also studied pressure drop and heat transfer characteristics of turbulent flow in annular tubes with internal wave-like longitudinal fins. The fins tested varied from 4-20 around the circumference of the inner pipe with Reynolds numbers ranging from 857 – 14710. Yu had conclusions similar to that of Wang.

Zamankhan [11] used the κ-ε, κ-ω and LES models to numerically simulate flow in a pipe with heat transfer enhancement features being helical turbulators. The presence of the turbulator was found to increase the heat transfer, sometimes without inducing turbulence, but

also increased the pressure drop. Zamankhan proved that the κ-ε model accurately predicted the flow within the pipe and is less computationally expensive compared to the κ-ω model. This is because the realizable κ-ε model performs well with rotational flow, strong pressure gradients, separation and recirculation. Agrawal et al. [12] used helical wires in the center tube to enhance the heat transfer for the fluid flowing in an annulus. The experiments tested different wire diameters (0.65mm, 1.0mm and 1.5mm) and different pitches (6.5mm, 10.0mm and 13mm). The helical wires were found to increase the heat transfer coefficient by as much as 100% of the plain tube value. Agrawal et al. also compared the coiled wire enhancement features compared to twisted tape heat transfer enhancement features presented by Lal [13] and it was shown that for the same mass flow rate the coiled wire does generate higher heat transfer. This reason is due to the disruption of the laminar sub-layer of liquid film and increasing the degree of flow turbulence.

Braga et al. [14] goes into detail the experiments tested using hot fluid (water) flow through the center tube and cold fluid (air) flow through the annulus using longitudinal rectangular fins on the inner surface of the annulus to enhance the heat transfer. There were 20 fins going around the circumference of the inner tube and Reynolds numbers tested ranged from 10,000 – 50,000.

Eiamsa-ard et al. [15] studied the influence of heat transfer in a tube with regularly-spaced helical tape swirl generators. Here hot air passed through the center tube which had the twisted tape inside and cold water passed through the annulus between the outer tube and the inner tube. The swirl flow devices consisted of: 1) the full-length helical tape with or without a centered-rod and 2) the regularly-spaced helical tape. With a Reynolds number range of 2,300 – 8,800 it was seen that the Nusselt number increased to a maximum of 50% above the plain tube.

Different pitches (0.5, 1.0, 1.5 and 2.0) were tested for the helical tape. The full length helical tape with rod provided the highest heat transfer due to the higher velocities that were seen due to the constricted passageway.

There were even cases of heat transfer seen where the shell and tube heat exchanger had a single-helix corrugated inner tube to help generate greater turbulence Withers [16]. Vicente et al. [17] had a heated inner tube that had dimples arranged in a helical fashion with different geometric parameters.

Ozceyhan [18] performed numerical work on flow through a heated pipe with ring heat transfer enhancement features. These rings are spaced with different pitches of 0.5, 1.0, 1.5, 2.0 and 3.0 times the size of the pipe diameter. The rings had a diameter of 5.7% of the pipe diameter. With Reynolds numbers ranging from 4,475-43,725 it was found that the best heat transfer enhancement ratio of 18% happened at a Re number of 15,600 with the spacing of the rings being 3.0 times the pipe diameter. Taylor et al. [19] also did numerical simulations for ribs on the inner surface of a pipe. The ribs were rectangular and had a rib spacing of p/e = 10. A Reynolds number of 15,000 was tested and heat transfer enhancement was found for this investigation as well.

Akpinar [20] had helical wires of different pitch mounted to the inner pipe in a double pipe heat exchanger and experimentally analyzed the heat transfer and friction factor. Hot air flowed through the inner pipe and cold water through that of the annulus. With a wire diameter of 4mm, the pitch were chosen to be 9, 15 and 21mm. Reynolds numbers were tested between 6,500 – 13,000 and it was found that Nusselt number and friction factor were as much as 2.64 and 2.74 times that of that of the empty pipe, respectively.

Rashkovan et al. [21] numerically optimized ribs in an annular gap by changing the rib height, pitch and width on the inner tube. The simulations performed used a modified κ-ε turbulence model. Rashovan said that the model was used in order to make it possible to predict flow separation, flow reattachment and adverse pressure gradients. To validate the use of this model he compared how κ-ε, κ-ω and RSM compared to the DNS work done by Ashrafin et al. [22]. Rashkovan found that as the width-to-height ratio decreases, the optimal pitch decreases as well but the rib-to-rib for maximum friction remains the same at above w/e =~6.

For a shell and tube heat exchanger with hot water running through the inner tube and cold water flowing through the annulus, Thianpong et al. [23] used a dimpled inner tube with a twisted tape swirl generator to enhance the heat transfer. Reynolds numbers ranged from 12,000 – 44,000, pitch ratio for the dimpled surface were 0.7 and 1.0 and twist ratio for the tape being 3, 5 and 7. The experimental results showed that both heat transfer and friction factor in the dimpled tube fitted with the twisted tape are higher than those in the dimple tube acting alone and plain tube. Both heat transfer and friction factor increase as the pitch ratio and twist ratio decrease.

Non-Annulus Heat Transfer Enhancement

There are numerous other types of internal cooling that are used for high thermal load applications. Pin-fins, dimples (negative features), and hemispherical protrusions (positive features, pimples) are some of the more common types of heat transfer enhancement features other than turbulators.

Maurer [24] investigated and reported all types of dimples for cooling purposes from numerous papers. Table 2.2 shows these references and the parameters that studied. Almost all of

these studies were experimental with Reynolds numbers ranging from 5,000-380,000. The aspect ratio of the dimples varied in size from 1:1-12:1. The depth to diameter ratio also varied with these studies with shallow dimples being less than 0.1 and anything greater being a deep dimple. Different patterns were studied and are shown in Figure 2.2.

Table 2.2: Investigation on dimpled cooling channels

Reference	Configuration	Aspect Ratio	H/D	δ/D	Pattern	Re_D	Type
[15]	one sided two sided	12:1 4:1 2:1	0.33 1 2	0.25	rectangular	15,000 - 35,000	Exp.
[39]	one sided two sided	-	1 2	0.25	rectangular	23,000 - 46,000	CFD
[44]	one sided	16:1 7.4:1 5.1:1 3.8:1	0.37 0.74 1.11 1.49	0.19	rectangular	12,000 - 60,000	Exp.
[41]	one sided	8:1	0.5	0.2	square	19,000 - 115,000	Exp.
[9]	one sided	4:1	1	0.2 0.3	square	21,000 - 124,000	Exp.
[8]	one sided	4:1	1	0.1	square	21,000 - 124,000	Exp.
[22]	one sided	4:1	2	0.3	square	5,000 - 40,000	Exp.
[60]	one sided	1:1	4.88	0.29	rectangular	7,000 - 21,000	Exp.
[45]	one sided	1:1	2.65 2.86 3.31 3.97	0.134 0.167 0.191 0.204 0.226 0.250	rectangular	10,000 - 65,000	Exp.
[33]	one sided	4.18:1	0.75	0.2	rectangular	120,000 - 380,000	Exp.

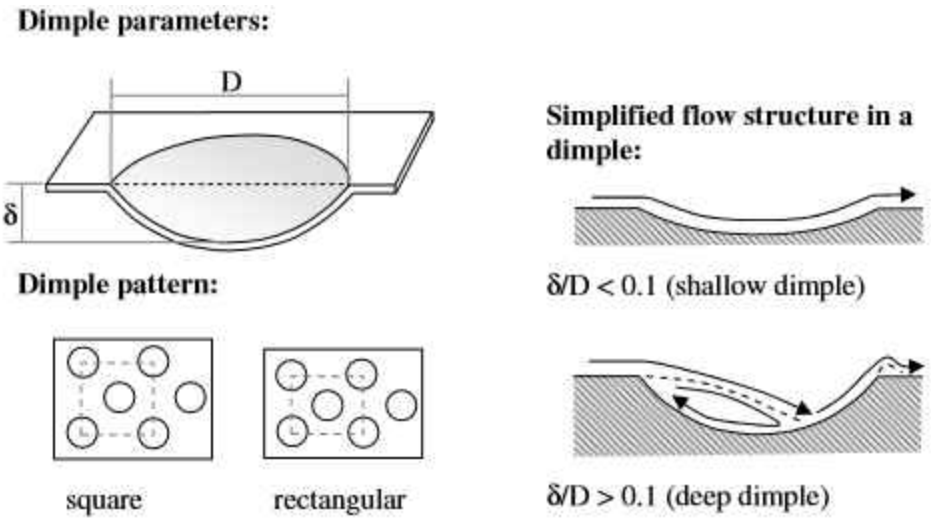

Figure 2.2: Dimple parameters and simplified flow structure in a dimple

Hemispherical protrusions are the opposite of dimples, the goal for these features is to again trip the laminar flow close to the wall causing it to become chaotic and mix with the passing flow. The typical flow pattern of these is shown in Figure 2.3 where there is a recirculation zone after the hemisphere and horseshoe vortexes sliding around the perimeters of the hemispheres. Moskvina et al. [25] studied the heat transfer and friction factor of hemispheres. The roughness density L/d_0 varied from 8 to 8.5 and the roughness height-to-hydraulic diameter k/D_h was 0.043 and 0.0635. A heat transfer augmentation of 90% was detected and accompanied by a friction factor enhancement, which was two-times higher than the friction factor of a smooth surface.

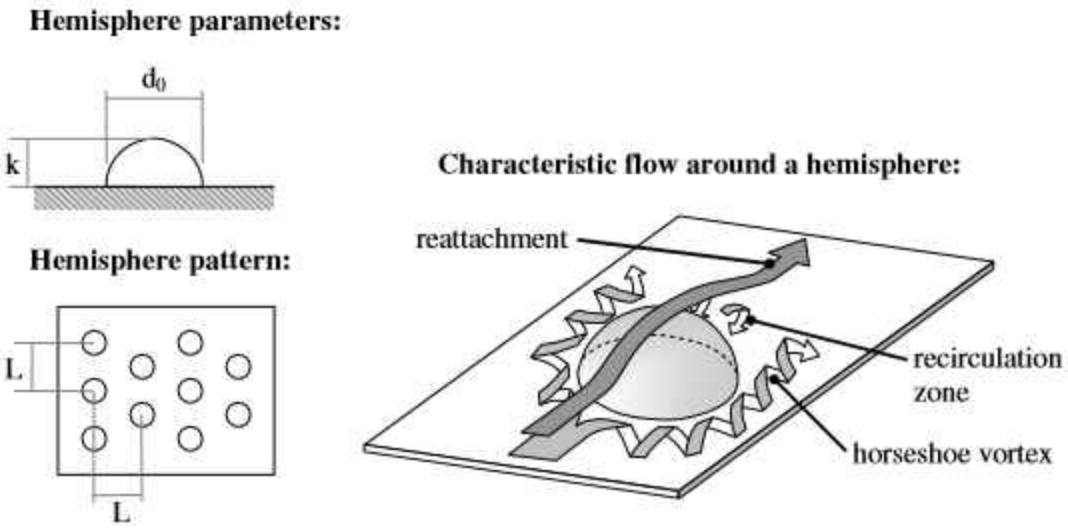

Figure 2.3: Parameters and characteristic flow field of a hemisphere

Impingement Cooling

Impingement cooling is one of best forms of cooling to generate the highest heat transfer. Flow travels through perforated surfaces creating a "jet stream" which hits a heated surface causing a thin boundary layer at the stagnation region to occur which promotes high heat transfer rates. High thermal stresses can occur because of this so precise location for impingement cooling is key to provide evenly distributed thermal stresses and cooling.

Florschuetz et al. [26] [27] is one of the most well-known and cited literature there is among impingement cooling. The work completed by Florschuetz et al. was performed with the goal of finding the optimum lateral and streamwise jet spacing, Y/D and X/D, in order to maximize the target wall heat transfer. For their studies, streamwise spacings of X/D = 5, 10 and 15, along with spanwise spacings of Y/D = 4, 6 and 8 were tested at jet-to-target wall spacings ranging from Z/D = 1-3. Additionally, jet average Reynolds numbers tested ranged from 5,000 to 50,000. This works major contribution comes in the form of a correlation for pitch averaged

Nusselt numbers as a function of the flow and geometric parameters of the channel shown in Eq. 2.11.

$$Nu = ARe_j^m\{1 - B[\frac{ZG_e}{DG_j}]^n\}Pr^{1/3} \tag{2.11}$$

Where A, m, B, and n are all dependent on the geometric spacing of the jets in the channel and whether the jets are in line or staggered. Furthermore, a one dimensional analytical flow model was also developed, which gives the local jet mass flux to average jet mass flux ratio as well as the cross flow mass flux to local jet mass flux ratio are displayed in Equations 2.12, 2.13 and 2.14, respectively.

$$\beta = \frac{C_D\sqrt{2}\pi/4}{\frac{YZ}{DD}} \tag{2.12}$$

$$\frac{G_j}{G_{j,avg}} = \frac{\beta N_c \cosh(\beta\frac{x}{x_n})}{\sinh(\beta N_c)} \tag{2.13}$$

$$\frac{G_c}{G_j} = \frac{1}{\sqrt{2}C_D}\frac{\sinh(\beta(\frac{x}{x_n}-\frac{1}{2}))}{\sinh(\beta\frac{x}{x_n})} \tag{2.14}$$

In these equations, the term C_D is the discharge coefficient calculated using the isentropic flow relations. These equations are useful for trying to understand the varying flow distribution in the channel as well as the relative strength of the crossflow compared to the mass flux of the jet.

C. Lee et al. [28] used transient liquid crystals to capture the local heat transfer of a single impingement jet hitting a concave semi-spherical surface. Jet Reynolds numbers ranged from 11,000-50,000 with the Z/D varying from 2-10 and the impingement angle varying from 0°-40. They found that the Nusselt at the stagnation point decreases as the tilt angle increases with a maximized result occurring at L/d = 6. Maximum heat transfer coefficients occur far from the

stagnation point as the tilt angle increases or the distance between the impingement jet and target surface decreases.

Yang et al. [29] studied the effect of having different shaped slot nozzles impinge on a semi cylindrical surface. Out of the round shaped nozzle, rectangular shaped nozzle and 2D contoured nozzle, the rectangular shaped nozzle resulted in an earlier increase in stagnation point Nusselt number as the nozzle to target surface spacing is increased. The jet flow is developed earlier for this case causing the turbulence intensity to increase sharply due to the sharp nozzle edge. The effect of the curvature of the target surface becomes more prominent when the Reynolds number increases.

Kumar et al. [30] presented some interesting work where flow passes through a cylindrical plenum and impinges into a semi-annular concave section where the target wall has effusion holes. CFD was performed to study the flow and heat transfer characteristics from five rows of circular impingement jets and four rows of effusion holes with in-line and staggered configurations for a jet Reynolds number of 7,500. The boundary conditions for this case are shown in Figure 2.4.

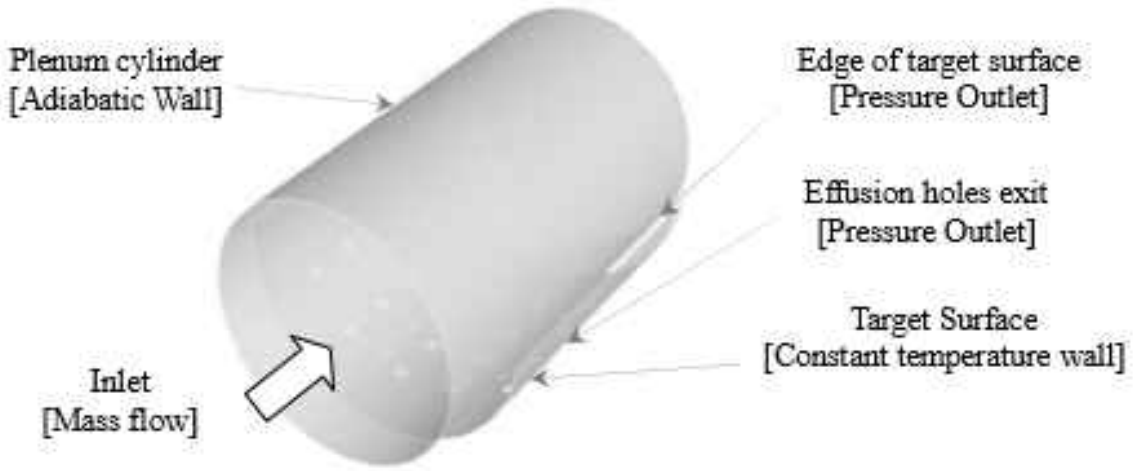

Figure 2.4: Boundary Conditions

Four different boundary conditions for the outlet were examined; all of the target surface edges were open, two edges were open, one edge was open and no edges were open. For all of these cases flow was exiting through the effusion holes as well. The case where there was only one edge outlet was the only case where the in-line impingement and effusion hole configuration produced higher heat transfer due to the cross-flow effect. The cases where no edges are blocked and all edges are blocked have a significant increase in the averaged Nusselt number when the formation is staggered as opposed to in-line with the highest heat transfer of all the cases occurring when all the edges are blocked.

The leading edge of a gas turbine blade experiences high temperatures which is why impingement cooling is needed to preserve the integrity of the blade. Iacovides et al. [31] studied the thermal development of a row of cooling jet impinging on a rotating concave surface, similar to the type of geometry that would be in a leading edge. Liquid-crystal technique was used to capture local Nusselt numbers with a jet Reynolds number of 15,000. The finding show that rotation causes the secondary peaks of each impingement jet to be non-existent and even some

primary peaks resulting in a decrease in heat transfer as opposed to no rotation. This is because the rotation increases the spreading rate of the jets, so much that the jet's core completely disappears within the first diameter from the jet exit. A possible cause is the generation of swirl by the Coriolis force, as the jets expand.

Cornaro et al. [32] investigated the flow visualization of an impingement jet hitting convex and concave surfaces. A constant Reynolds number of 6,000 was tested along with a varying Z/D of 1, 2, 3 and 4. For Z/D = 2, small vortices appear on the wall and maintain integrity for quite a distance from the stagnation point before breakdown. Based on the diameter of the jet, the duration of these stable coherent vortex rings can be seen up to 60° along the surface. Flow over a concave surface is more unsteady than flow on a convex surface as the flow upstream of the concave surface is strongly affected by the flow exiting the surface into recirculation. This exhaust flow becomes entrained in the primary jet flow, reducing the likelihood of stable ring vortices.

Tawfek [33] studied the effect of jet inclination of a circular impingement jet hitting a cylindrical convex surface. The jet Reynolds number, jet inclination angle and Z/D ranged from 30,000-40,000, 20°-90° and 7.5-30, respectfully. Circumferential heat transfer as well as axial Nusselt number were calculated. The point of maximum heat transfer along the x-axis is shifted upstream and the local heat transfer distribution changed depending on the inclination angle of the jet. This shift had a much higher heat transfer distribution compared to that of the flat plate. It was seen that increasing the jet inclination cause the heat transfer to become asymmetric around the stagnation point with the upstream heat transfer dropping off quicker than that of the downstream.

Kayansayan et al. [34] investigated jet impingement cooling on a concave semi-circular channel using a slot-jet at slot width-to-surface ratios ranging from 2.2-4.2 for Reynolds numbers of 200-11,000. Experimental and numerical efforts were put forth for this study. A correlation for the stagnation point heat transfer was created based on 30 data points which is shown in Equation 2.15. The correlation is valid for Reynolds numbers between 1,000-10,000 and slow width-to-surface ratio (H) between 2.2-4 with a scatter of ±5%. It was found that heat transfer measurements at the stagnation region indicated that Nusselt number is not affected by the variation of the channel radius ratio however the Nusselt number does decrease as the channel spacing increases. Reynolds numbers for the numerical work only went up to 600 because the velocity fluctuations of wall jet flow along the concave surface which caused instability in the simulations. For the low Reynolds number computational cases, a maximum of 28% deviation between experimental and numerical was found for the circumferential Nusselt number at the stagnation region.

$$Nu = 2.6Re^{0.386}H^{-0.445} \tag{2.15}$$

Cornaro et al. [35] used TLC to find local heat transfer for jet impingement on a convex semi-cylinder. Z/D ranged from 1-4 with a Reynolds number of 6,000-16,000 was tested. Finding show that peak heat transfer was found at 0.5 times the diameter away from the stagnation point along the longitudinal axis of the semi-cylinder. Cornaro also found that the heat transfer decreases monotonically until the length traveled about the curvilinear axis is greater than 1.2 times the jet diameter. The Nusselt number then increases along this direction in the region between 1.3 and 2.2 times the jet diameter until it reaches a maximum. The intensity and the location of this maximum are related to the Reynolds number and the jet exit-to-surface

distance and are caused by a transition in the boundary layer. In conclusion, it was found that heat transfer increases with increasing curvature and Reynolds number as well.

Zuckerman et al. [36] did a comprehensive numerical study on impingement jets on a flat surface. He compared various criteria for numerous turbulence models which included the computational cost, how close it predicts actual Nusselt number values and the turbulence model's ability to predict the secondary peak in heat transfer. This secondary peak can be seen in Figure 2.5 and is caused by the local flow reversal, also known as separation. This turbulent region causes unsteadiness in the thermal boundary layer outside of the stagnation region that result in high heat transfer.

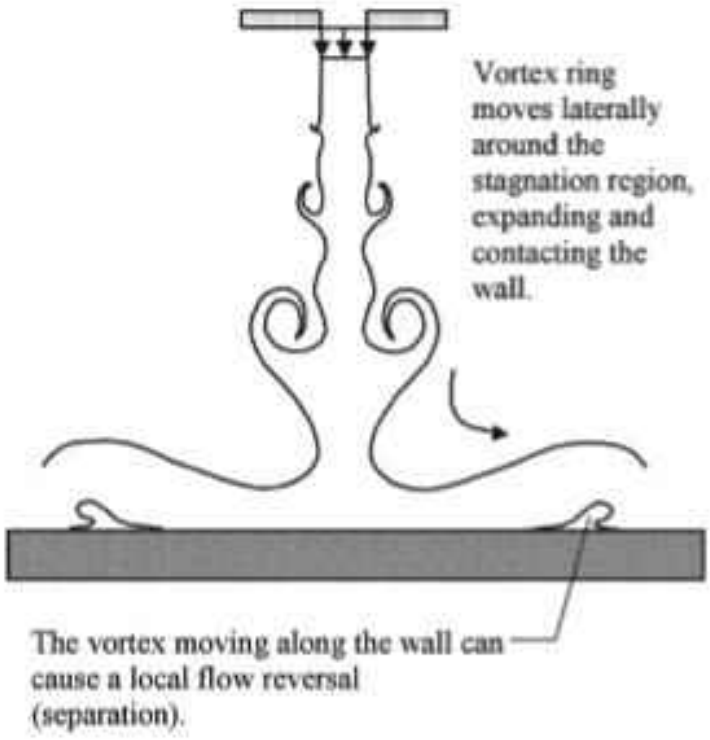

Figure 2.5: Secondary Peak in Impingement Flow

He concluded that the best performance of impingement jets occur at a region ranging from 2-8 H/D where the shear layers may interact. With all the numerical models studied, the SST and v^2-f

models offer the best results for the least amount of computation time, with the v^2-f being the superior with a typical Nusselt number error of 2-30%. The higher uncertainty is where the stagnation point of the impingement jet resides.

Choi et al. [37] did an experimental study of impingement jet heat transfer on a semi-circular concave surface. Reynolds numbers of 1,780, 2,960 and 4,740 and Z/D spacings of 4, 6 and 10 were tested. The potential core is the region where the centerline velocity remains almost constant. This region was investigated in this report. It was found that the potential core length becomes shorter at greater Reynolds numbers. The peak of the stagnation Nusselt number occurs at the spacing which is about equal to the potential core length with the stagnation region thickness equal to twice that of the jet diameter. The secondary peak was found to be closer to the stagnation point as the Reynolds number increases. An increase in the stagnation heat transfer rate for Z/D = 2-3 compared to 5-6 is due to the steep increase in velocity fluctuations measured in free and impinging jets.

Craft et al. [38] studied the flow and heat transfer of a row of 5 impinging jets onto a concave semi-circular surface. Experimental and numerical work was presented. A linear and non-linear k-ε turbulence model selected. The non-linear model produced slightly better turbulence stress levels, but both models under predicted the turbulence energy as the jets approach the curved surface and the downwash region. Heat transfer was under predicted around the jet to jet interaction as well.

CHAPTER 3: PURPOSE AND PROBLEM STATEMENT

There is a wealth of literature available for heat transfer enhancement inside a channel Han [39] or on the outside of a heated pipe by enclosing an annular flow path around it with features on the inside surface of the annulus Braga [14]. However, there is very little past work reported where heat is removed from the outer surface of an annular flow path that is formed inside a hot object. Many of the strategies that are deployed for removing heat from the inner surface of an annulus are not necessarily effective when heat is removed from the outer surface of an annulus. The focus of this study is to investigate the removal of heat from the outer surface of an annulus by a coolant flow through the annular flow path, with and without heat transfer enhancement features. Helical turbulators and potential centrifugal action created by helical flow will be utilized to remove heat from the non-turbulated outer heated surface.

As the body of knowledge in single-phase transport enhancement within annular ducts is limited, this study will add new understanding, especially in terms of how fluid mechanics can be exploited to provide higher heat transfer.

CHAPTER 4: NUMERICAL SETUP AND DATA REDUCTION

Physical Model

In order to investigate how the enhancement features affect the heat transfer and pressure drop within an annulus, there were geometric parameters that needed to be established. The parameters that were studied for this investigation were: the shape of the turbulator, the blockage ratio, e/h and the helix angle. In previous literature, Han et al. [39] performed numerous experiments using rectangular shaped turbulators to disrupt the flow. Ozceyhan [18] and Hossain et al. [40] used circular turbulators for their experiments. It was decided that both circular and square shaped turbulators will be used for this study to see how the shape of the turbulator can affect the heat transfer and pressure drop.

The blockage ratio was chosen to range between 0.24 and 0.56. Han et al. [39] compiled some work of other finding of ribs within a rectangular duct in which the ribs varied in blockage ratio from 0.02 by Momin et al. [41] up to 0.094 by Al-Hadrami et al. [42]. The blockage ratio for this study is a lot larger than what other literature of turbulators suggests. There are two reasons for this. 1) For ribs within a rectangular duct, the blockage ratio usually does not exceed 10% of the channel height. This is because the pressure drop significantly increases and the pros for the heat transfer are being outweighed by the cons for the pressure drop. As the increasing blockage ratio occurs the flow within that channel becomes more and more constricted. If the turbulator/rib was to be the channel height the flow would be unable to pass. However, in an annulus, with the angles turbulators residing in a helical fashion, even if the turbulator height was the gap height, flow would still be able to pass through the annulus by swirling as the flow travels further downstream. If the turbulator height in an annulus was similar to that of a channel,

there would be little to cooling enhancement happening on the outer pipe. This would only trip the flow but due to the strong cross flow happening in the annulus, the turbulent/chaotic flow due to the turbulators would stay right along the inner pipe. 2) The main goal is to increase the heat transfer on the outer pipe. With a larger blockage ratio for the turbulator, this would create more of a helical swirling flow as it follows the route of the turbulator downstream. This flow would be traveling in an outward motion from inner pipe due to the centrifugal effect of the spiraling colder fluid and would remove heat from the non-turbulated outer heated surface.

When looking at the literature for angled ribs inside a channel the typical turbulator angle (α) ranges from 30°-60°. There are even cases where the turbulator angle is quite large, such as in the case for Momin et al. [41] where he investigated angles up to 75°. For this study, the helix angle of the turbulators was chosen to encompass angle from 15°-30°. The reason for having the angle smaller than literature for channel flow is to try to help simulate the swirling effect of the flow to help promote the centrifugal effect to push colder flow out towards the hot surface. In the case, if the angle was 0°, it would act like ring turbulators. Likewise, if the angle was 90°, it would act like stream-wise turbulators.

The parameters were chosen to be manually changed by averaging cases to produce offspring and further optimize the design until there were no geometrical changes to perform. Figure 4.1 shows how this was done. Parameters a-d were pitch values representing helix angles of 15°, 20°, 25° and 30° respectively and parameters e-g were blockage ratios of 0.3, 0.5 and 0.7 respectively. In order to properly mesh the fluid domain, the turbulators had to merge 20% into the inner pipe to prevent high skewness angles, especially for the circle turbulator cases. Figure 4.2 shows how these turbulators were configured with the wall. This merger resulted in the blockage ratios becoming 0.24, 0.4 and 0.56 for parameters e-g respectively.

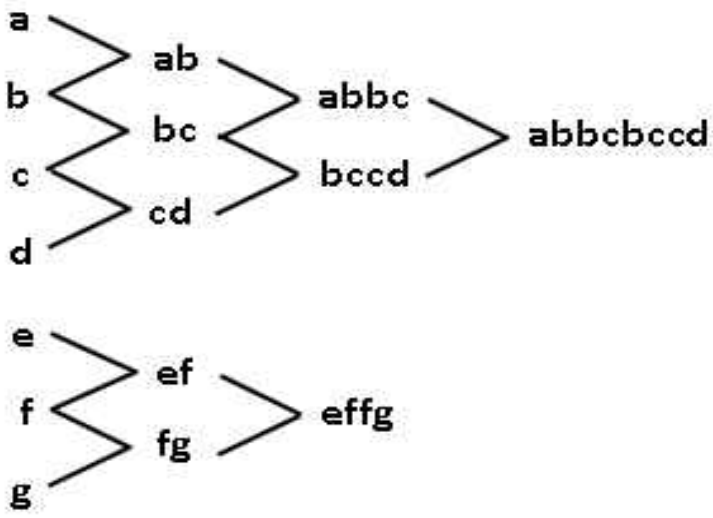

Figure 4.1: Geometric Parameter Lineage

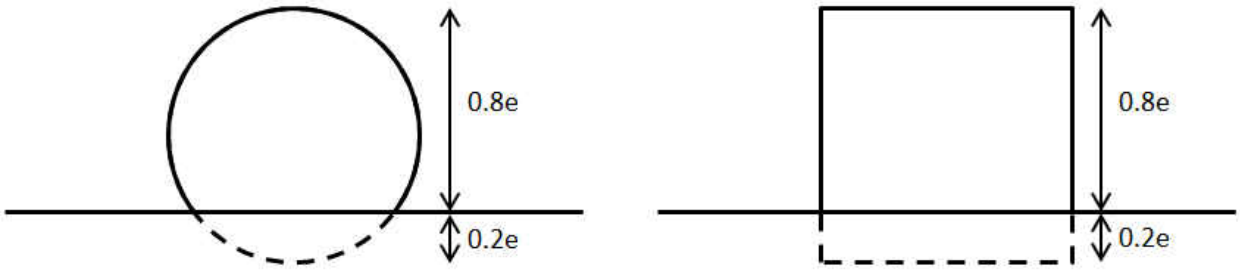

Figure 4.2: Turbulator Attachment to Inner Annulus Wall

Figures 4.3 and 4.4 show the helicoil turbulators and the cross section for the annular flow, respectively. Kays et al. [6] determined that annular flow becomes fully developed at ~18D_h. Based on that knowledge, a flow developing region before the turbulators was chosen to be 20D_h. The same length of straight double pipe was chosen after the turbulators as well to re-establish the flow. The annular diameter ratio (Di/Do) for this experiment was set to 0.92. Having a larger diameter ratio causes the flow velocity to be greater and will have a stronger

impact on heat transfer compared to a lower annular diameter ratio. To reduce the computational time, a 45 degree portion of the annulus was chosen for the testing domain.

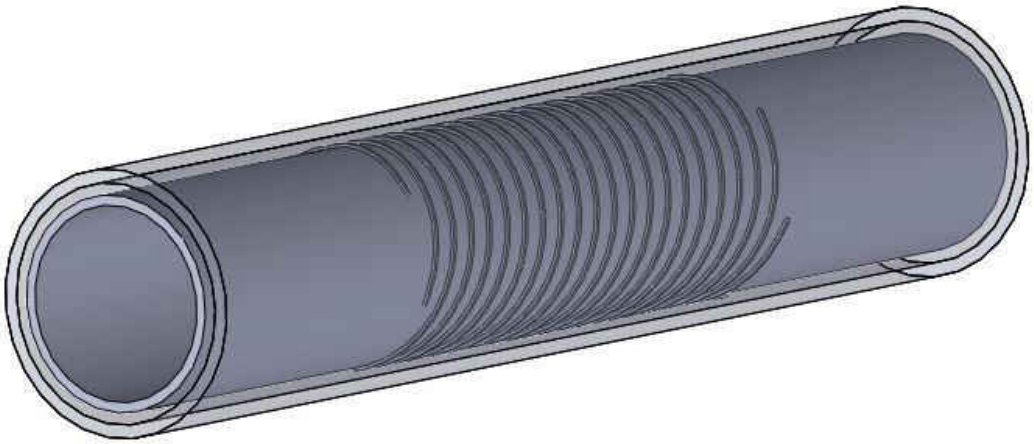

Figure 4.3: Concentric Pipe with Helical Turbulators

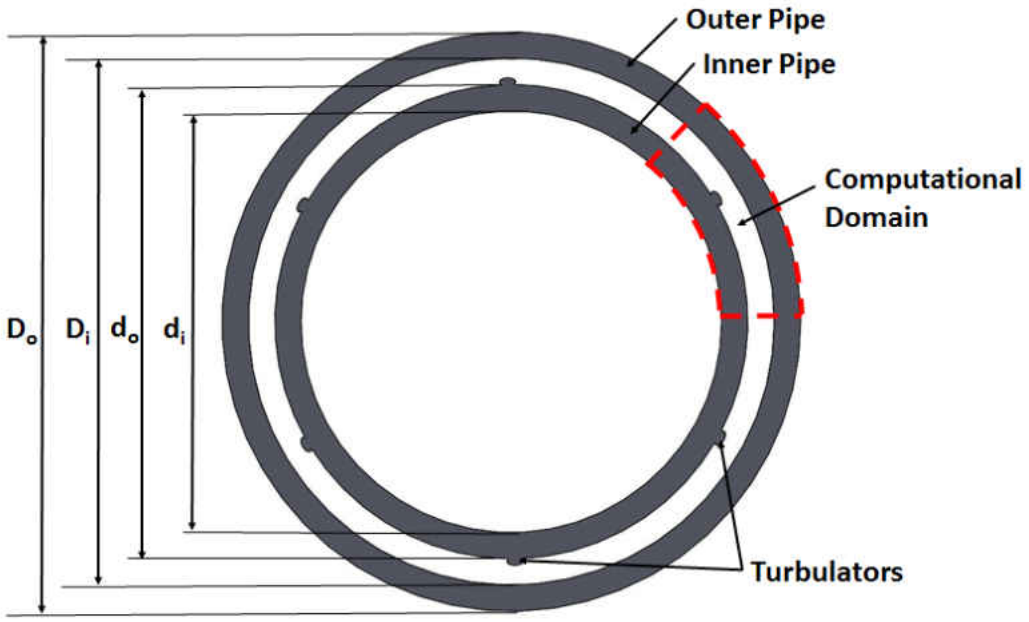

Figure 4.4: Schematic of Cross-Sectional View of Annular Duct with Turbulators

Figure 4.5 shows the nomenclature that was used for the geometric parameters that were changed for each design. The turbulator height, e, the helix angle, α and the pitch, p varied in dimension. The annular gap height, h was held constant for all the numerical cases.

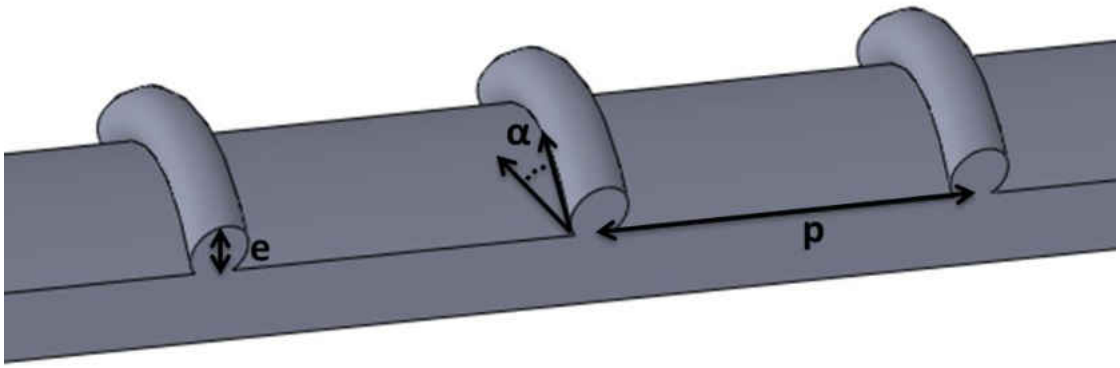

Figure 4.5: Geometric Parameter Nomenclature

A test matrix, shown in Table 4.1, was composed of a baseline case which had no turbulator enhancement features and then 50 cases of each circle and square turbulators.

Table 4.1: Test Matrix

Turbulator Shape	**Blocking Ratio (e/h)**	**Helix angle (α)**	**Reynolds Number**
Square/Circle	0.24-0.56	15°-30°	25,000

Boundary Conditions

For this study, the boundary conditions can be seen in Figure 4.6. A constant inlet temperature of 300K was used. The outer pipe had a heat flux of 5.0 W/in^2 (7750 W/m^2). This region covers the sections before and after the turbulated section as well as the turbulated region of interest. A flow developing section was used before the helicoil turbulators to establish uniform flow entering the turbulated section, and a flow recovery section was included after to help recover pressure loss from the heat transfer enhancement features. The inner pipe and turbulators were nonparticipating for heat transfer (adiabatic boundary condition). Symmetry was claimed for each side of the 45 degree annulus region. A pressure outlet boundary condition was used for the outlet. A target mass flow rate indicator was created and reached for all cases. Each case had to be within a 1% uncertainty of the desired mass flow rate to be accepted as a viable case for the study.

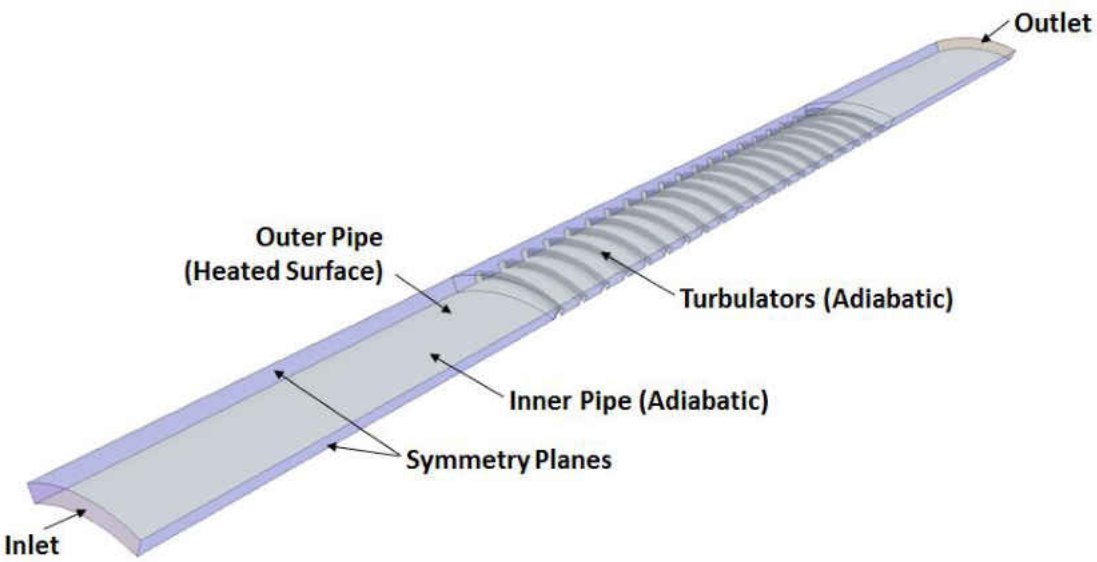

Figure 4.6: Boundary Conditions for Fluid Volume

The mass flow rate was determined by using a constant Reynolds number of 25,000. The hydraulic diameter of the annulus (without turbulators) is used as the characteristic length. Equation 4.1 is used to calculate Reynolds number.

$$Re = \frac{\rho D_h}{\mu} \tag{4.1}$$

The heat transfer coefficient, htc and Nusselt number, Nu were both found using the local bulk temperature of the fluid. These two formulas are listed below as Equation 4.2 and 4.3, respectively.

$$htc = \frac{q"}{(T_w - T_b)} \tag{4.2}$$

$$Nu = \frac{htcD_h}{k} \tag{4.3}$$

Computational Mesh and Numerical Modeling

The mesh and numeric solving was performed using a commercial solver called STARCCM+. A mesh sensitivity analysis was performed on the control volume to determine that the solution would not change based on the mesh refinement. The mesh sensitivity shown in Figure 4.7 ranged from 1.67-26.06 million cells. The averaged Nusselt number using bulk temperature varied 0.03% between the 26.06 and 4.66 million cell meshes so it was deemed that the 4.66 million mesh parameters will be used for all cases to save computational time. Figure 4.8 shows the mesh parameters used for all the simulations.

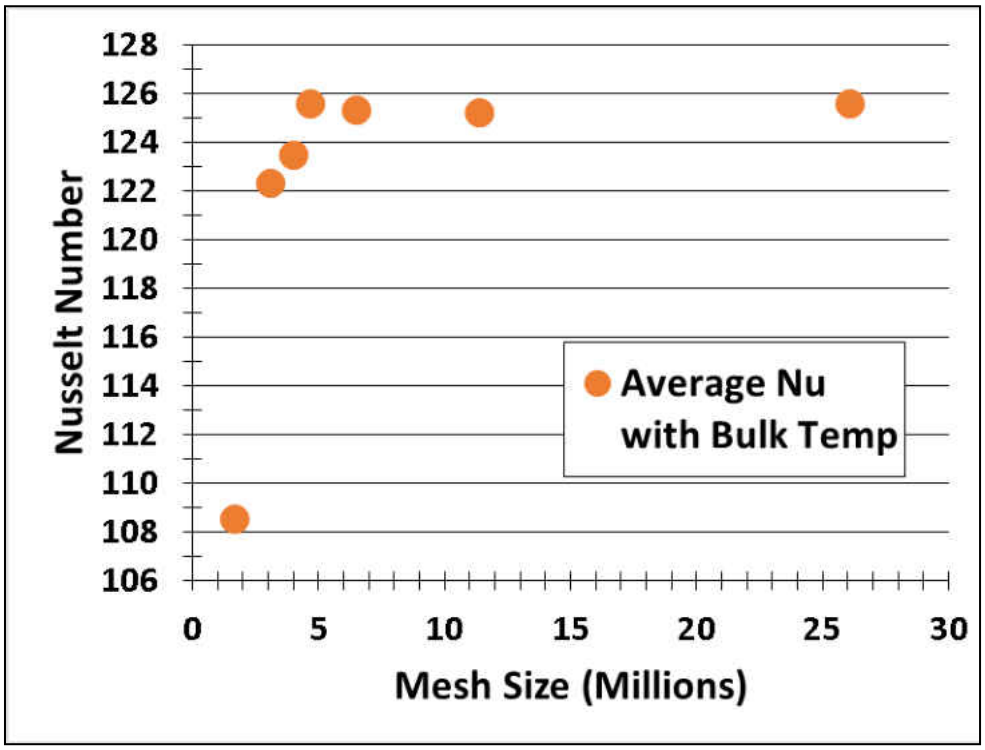

Figure 4.7: Mesh Sensitivity

Picking the correct turbulent model for numerical simulations is important for predicting accurate heat transfer data as well as saving computation time. Large Eddy Simulation (LES) and

Direct Numerical Simulation (DNS) are the desired solving methods to accurately predict flow and heat transfer; however, these solvers are computationally expensive and highly impractical for optimization at this point in time. Reynolds-Averaged Navier-Stokes (RANS) equations are used instead to predict flow and heat transfer distribution while saving computational time. The second order realizable ƙ-ε model was used for this optimization because it has been proven by Wang QW et al. [43] to properly simulate heat transfer and flow for internally longitudinally finned tubes and Zamankhan [11] used this model to observe turbulence near the wall for annular flow with helicoil turbulators. Zamankhan also studied the ƙ-ω model which took more cells to reach grid independence and thus took longer computational time. A segregated flow and fluid temperature solver were used for all the numerical calculations.

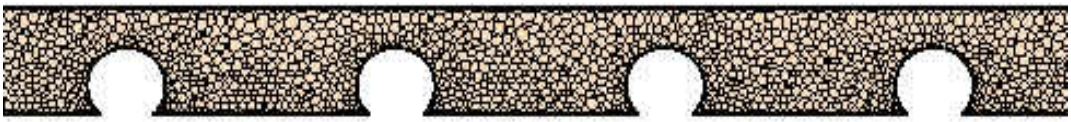

Figure 4.8: Mesh of Computational Cross Section for Turbulated Domain

There was a study done on a 3D backwards facing step that compared different types of mesh; polyhedral, tetrahedral and hexahedral cells. Volume element count, pressure drop and runtime were studied. The fluid domain and boundary conditions were held constant for all cases. The tetrahedral cells had the high density of 14.3 million followed by the hexahedral at 7.4 million and lastly the polyhedral cells at 2.7 million. There were minor differences in the converged pressure drop for all cases however the polyhedral case reached convergence much quicker than the rest. It took the polyhedral, hexahedral and tetrahedral cases 400, 550 and 900

iterations, respectively. With this being said, the tetrahedral had the longest runtime with the highest density of cells as well. The hexahedral case was just over 2 times as quick at solving and the polyhedral case solved the quickest at 4 times as fast as the tetrahedral case. The polyhedral mesh demonstrated that it could produce equivalent accuracy results as the other meshes but with faster convergence and fewer iterations. M. Peric [44] has done multiple studies on polyhedral meshing and the conclusion of those papers show the same results. For these reasons, the polyhedral mesh was chosen to cut down on computational time while still remaining accurate.

The polyhedral cell has more faces than hexahedral or tetrahedral cells which mean that it has more storage and computing operations per cell which means higher accuracy. This cell type is very beneficial for when there is recirculating flow like in a case where turbulators are present. For complex types of control volumes, polyhedral meshing is far superior to the other alternatives.

Prism layers are added near the wall to accurately predict the boundary layer. Prism layers allow to capture this phenomenon correctly while conserving the overall mesh size and run time allowing for good convergence and accurate results. Having a wall Y+ less than 5 allows for accurate prediction inside the laminar sub layer region where velocity profiles are assumed to be laminar and viscous stress dominates the wall shear. Figures 4.9 and 4.10 show the wall Y+ on the turbulator surface and target surface, respectively.

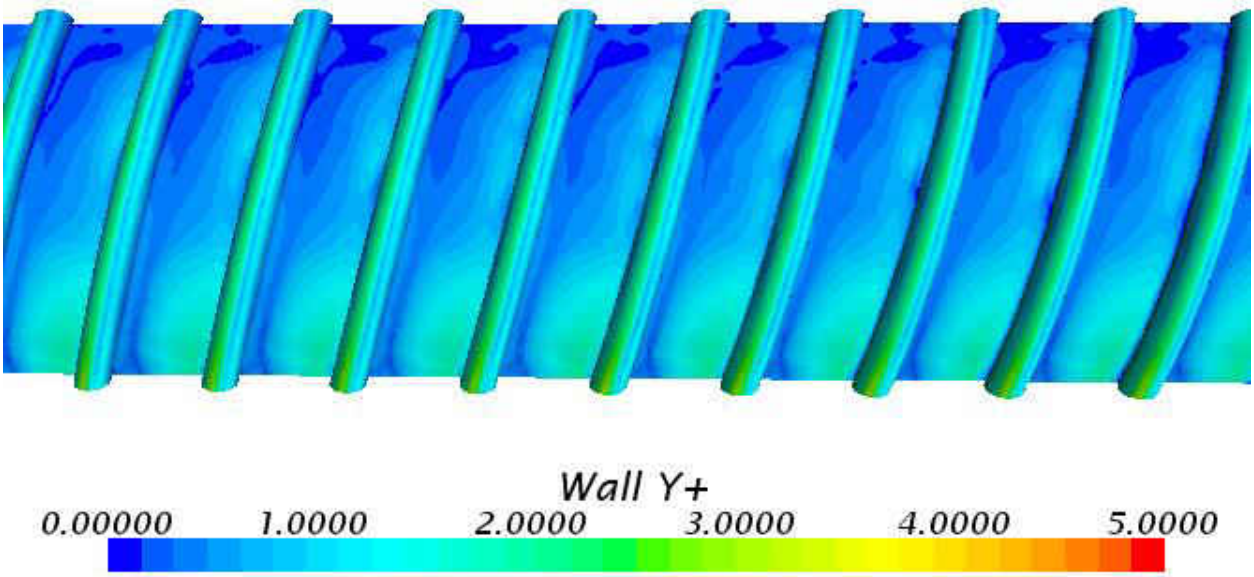

Figure 4.9: Turbulator Surface Wall Y+

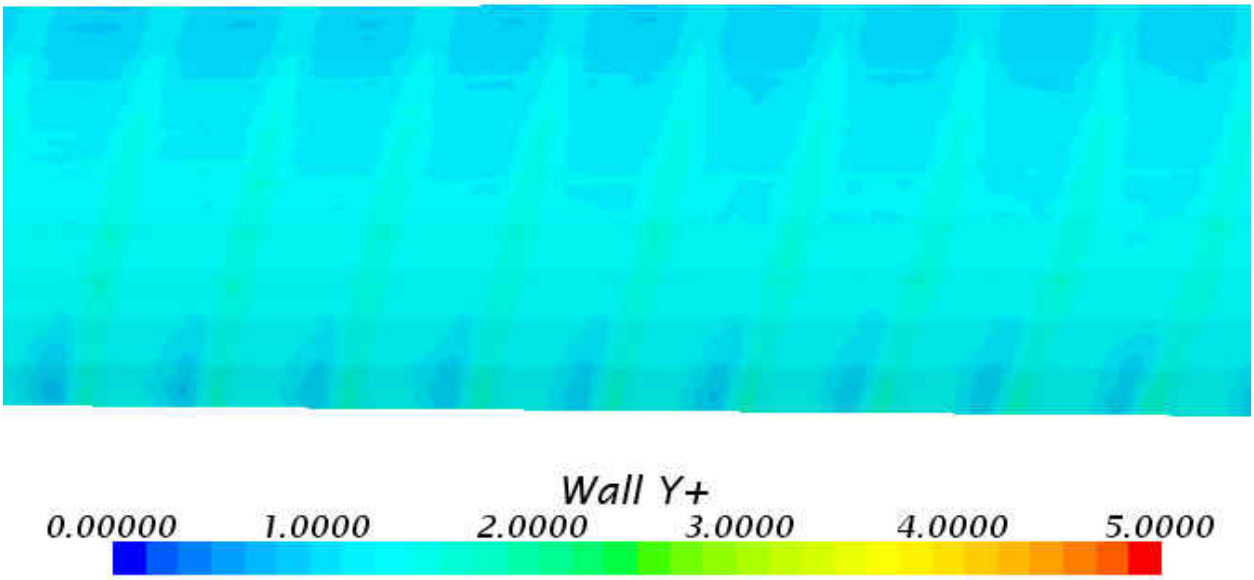

Figure 4.10: Target Surface Wall Y+

CHAPTER 5: NUMERICAL RESULTS AND DISCUSSION

As stated previously, the focus of this study was to investigate the removal of heat from the outer surface of an annulus by a coolant flow through the annular flow path, with and without heat transfer enhancement features. Observation of any potential effect of centrifugal action created by the helical turbulators to remove heat from the non-turbulated outer heated surface was also investigated.

With all of the cases for both circle and square turbulators completed, a Pareto front chart can be seen in Figure 5.1. This chart shows how the change in blockage ratio and shape of the turbulator can affect the pressure drop and Nusselt number. As the blockage ratio increased, the flow traveling downstream was constricted which caused the pressure and the swirling motion from the helicoil turbulators to increase.

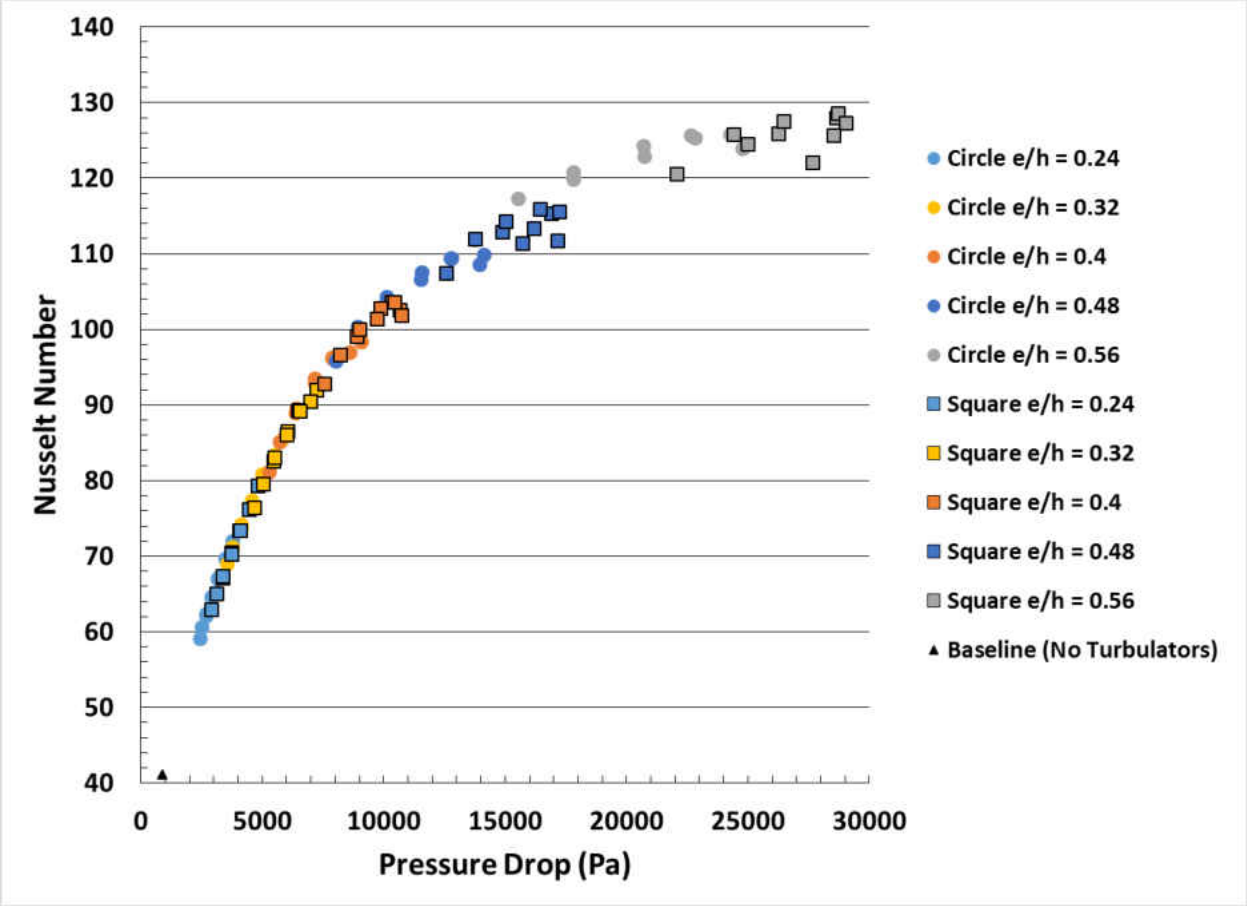

Figure 5.1: Pareto Chart for Nusselt Number vs. Pressure Drop

Figure 5.2 shows a schematic of typical flow and the types of flow features for flow passing over turbulators/ribs. In this figure it can be seen that separation of flow occurs as turbulent flow passes over the turbulators. With this separation of flow there will be a period of length in the trough between the turbulators where there will be reversal flow, also called recirculation. Given that the turbulator pitch is spaced far apart, there will be a point at which this separating flow will reattach with the wall and hug the wall until the next turbulator arrives. The flow will again be tripped and accelerated past this turbulator causing separation again and the flow will repeat this cycle for however many turbulators are left. Figure 5.3 shows how the shape and blockage ratio can affect the flow velocity for the same pitch. For a constant helix

angle of 30°, the blockage ratios of 0.24, 0.32, 0.40, 0.48, 0.56 caused increased velocity, respectively. As the blockage ratio increased there was a greater recirculation zone in between the turbulators. The high velocity going over the turbulators caused a pocket of high pressure underneath where flow gets recirculated. Due to the pitch of the turbulators, a swirling motion occurred as the flow traveled further downstream

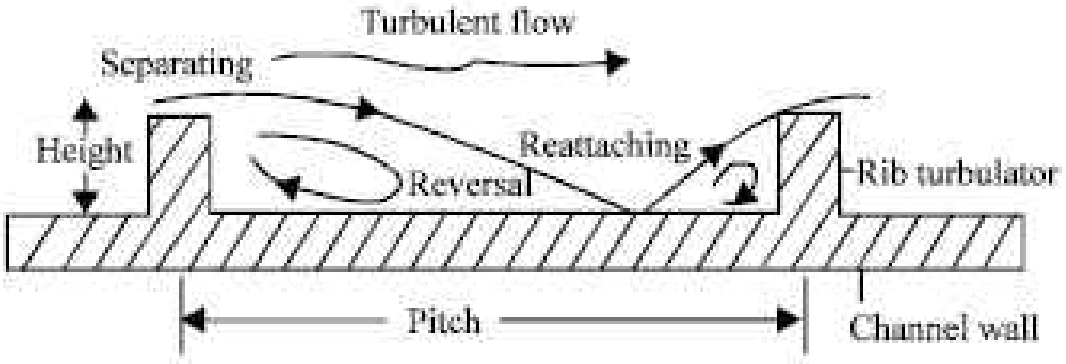

Figure 5.2: Schematic of Flow Field Over Turbulators

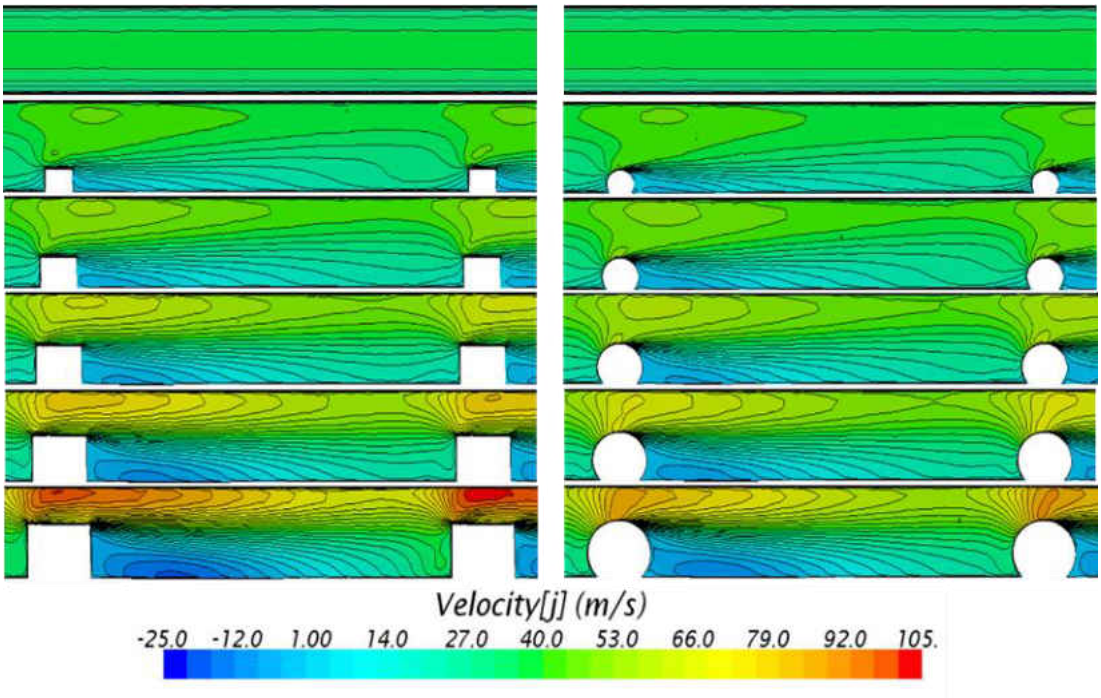

Figure 5.3: Velocity Cut-Plane for Increasing Blockage Ratios

The pitch of the turbulators was investigated for both circular and square shaped turbulators. In Figure 5.4, as the turbulators were increased over a range of helix angles (15°, 20°, 25°, 30°) while keeping e/h held constant at 0.56, the velocity and recirculation decreased as the helix angle is increased. The pressure drop increased as the pitch decreased.

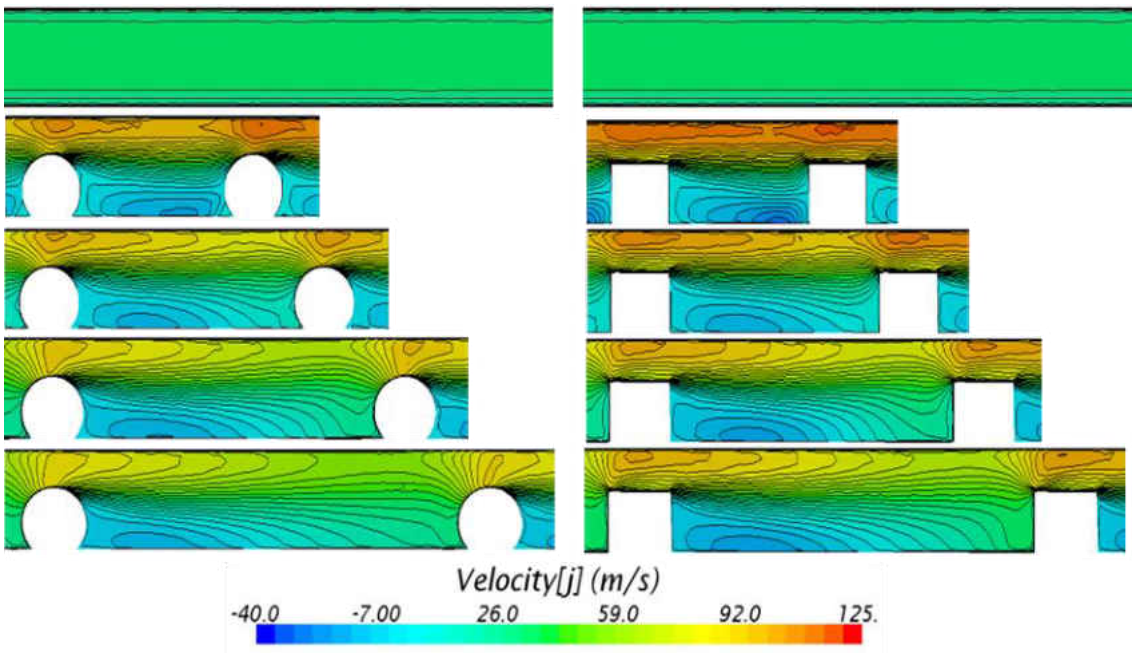

Figure 5.4: Velocity Cut-Plane for Increasing Helix Angles

Figure 5.5 shows how the Nusselt number was affected by the helix angle. As the helix angle (pitch) increased, the Nusselt number dropped. An increase in Nusselt number was seen for cases where e/h is at least 0.4 and a helix angle of 20°. This can be attributed to the recirculation of flow and the swirling effect in between turbulators as flow traveled downstream. The cases with the smaller blockage ratio were not able to contain a high pressure region in between the turbulators to cause the swirling motion seen by the rest of the higher blockage ratios. On average, the Nusselt number decreased by 1.0 and 0.62 for every percent increase in helix angle for circle and square turbulators, respectively. The average heated outer pipe surface temperature decreased 0.87 and 0.76 K for every percent increase in blockage ratio for circle and square turbulators, respectively. The circle turbulators have a greater change in surface temperature when compared to the square, but the square turbulators were more effective at cooling the surface temperature of the outer pipe.

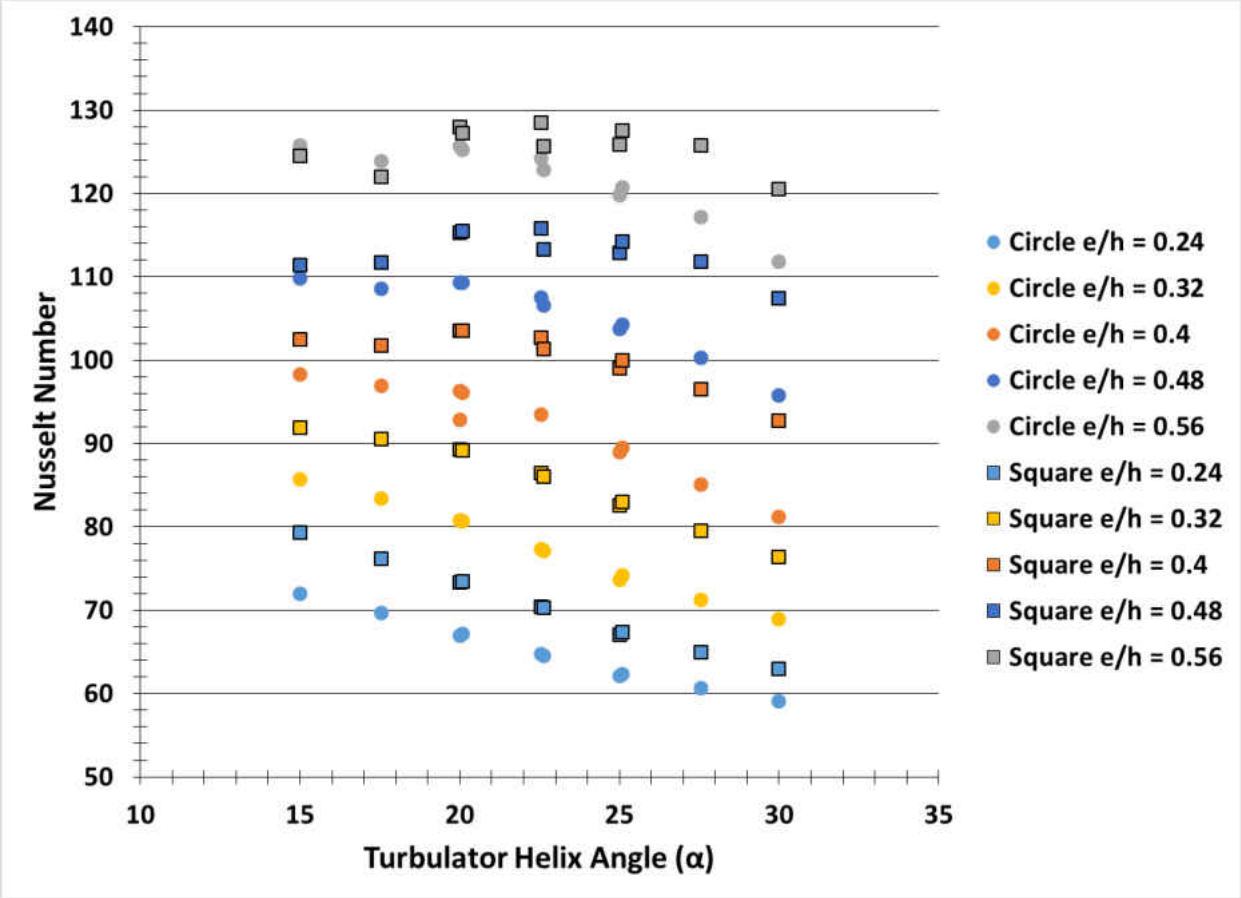

Figure 5.5: Nusselt Number vs. Helix Angle

Figure 5.6 shows the pressure drop corresponding to the helix angle. As the blockage ratio increased, the pressure drop increased exponentially. With a growing helix angle the pressure drop decreased in a linear trend for the cases where the blockage ratio was less than 0.40. Just like the Nusselt number, an increase in pressure drop occurred at a helix angle of 20° where the recirculation and swirl were most chaotic. An example of this swirling effect is depicted in Figure 5.7. The stronger velocity above the turbulators caused high pressure in between the turbulators which recirculated the flow as it swirled further downstream. The average pressure drop decreased 353 and 163 Pa for every degree increase in helix angle for both

circle and square turbulators, respectively. At higher blockage ratios, the square turbulator has a significantly larger pressure drop than that of the circle.

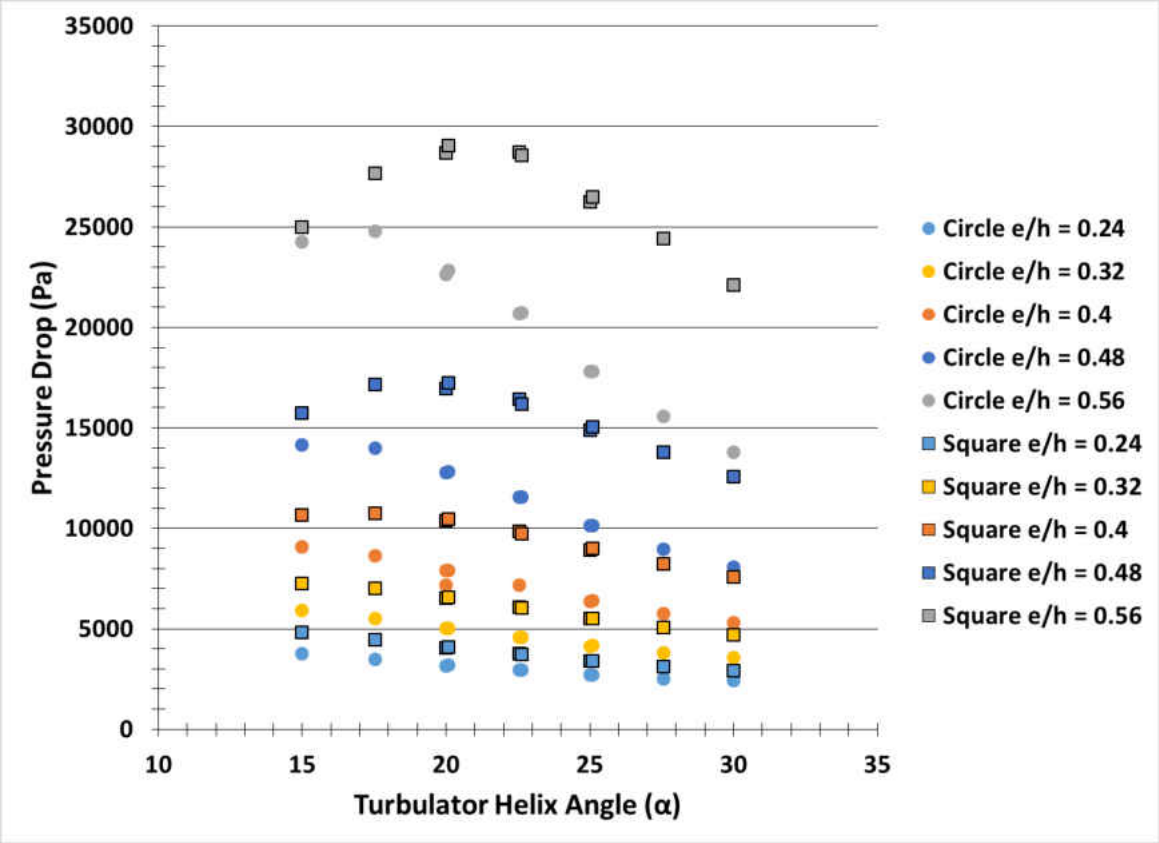

Figure 5.6: Pressure Drop vs. Helix Angle

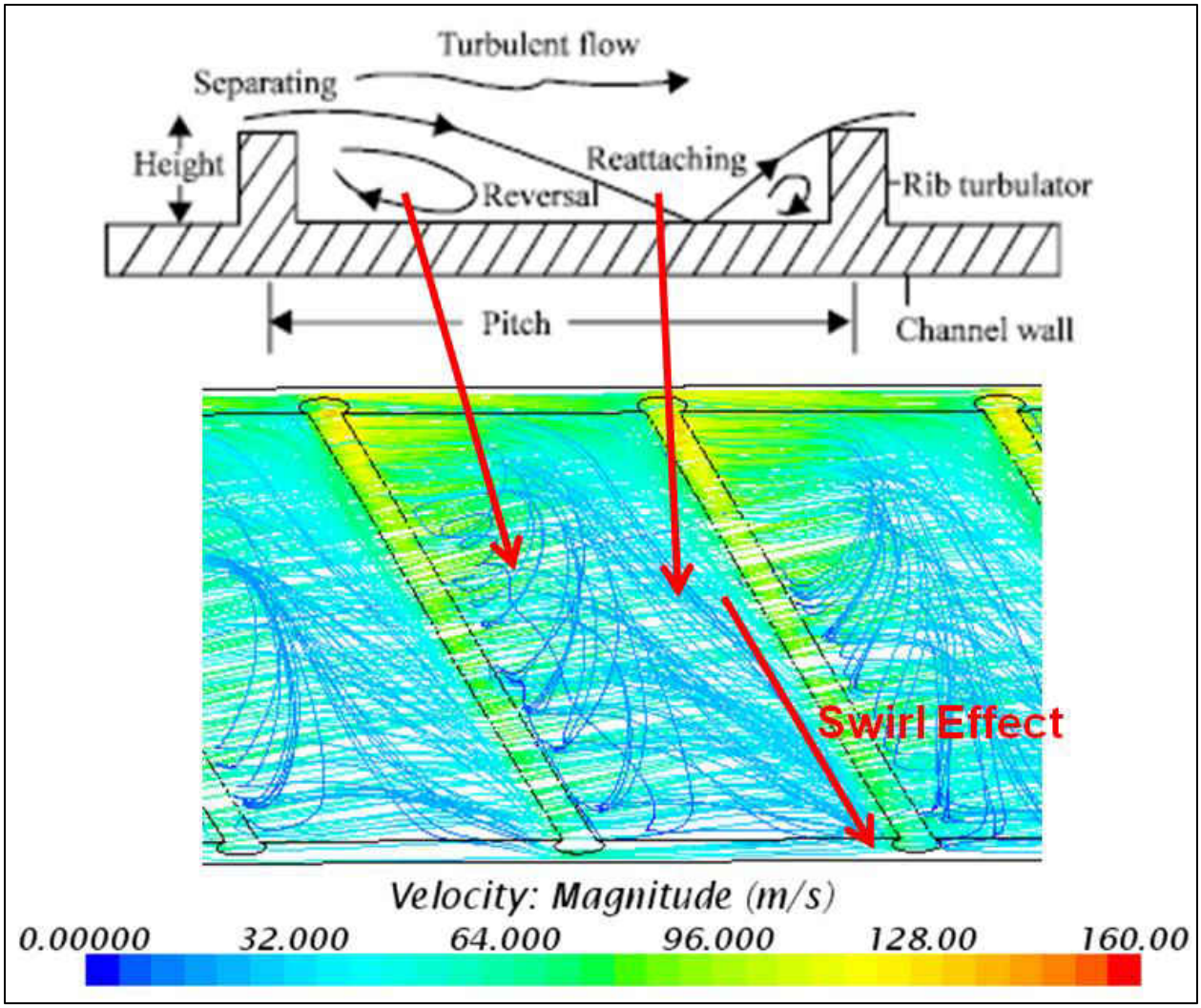

Figure 5.7: Swirling Effect as Flow Recirculates in Between the Turbulators and Travels Downstream

When looking at the impact of the blockage ratio to the Nusselt number, it can be seen in Figure 5.8. The Nusselt increased in a linear fashion as the blockage ratio was increased. The square shape had a greater increase in the Nusselt number compared to the circular shape. For every percent increase in e/h, the average Nusselt number increased roughly 1.71 for the circle and 1.77 for the square turbulators. The pressure exponentially increased with the increase in e/h as shown in Figure 5.9. On average, the pressure drop increased by 250 and 335 Pa for every

percent increase in e/h for circle and square turbulators, respectively. The square turbulators perform better than the circle at keeping the outer pipe cooled as the helix angle increased. The circle turbulator increased 0.55 K for every degree increase in helix angle as compared to the 0.38 K increase for the square.

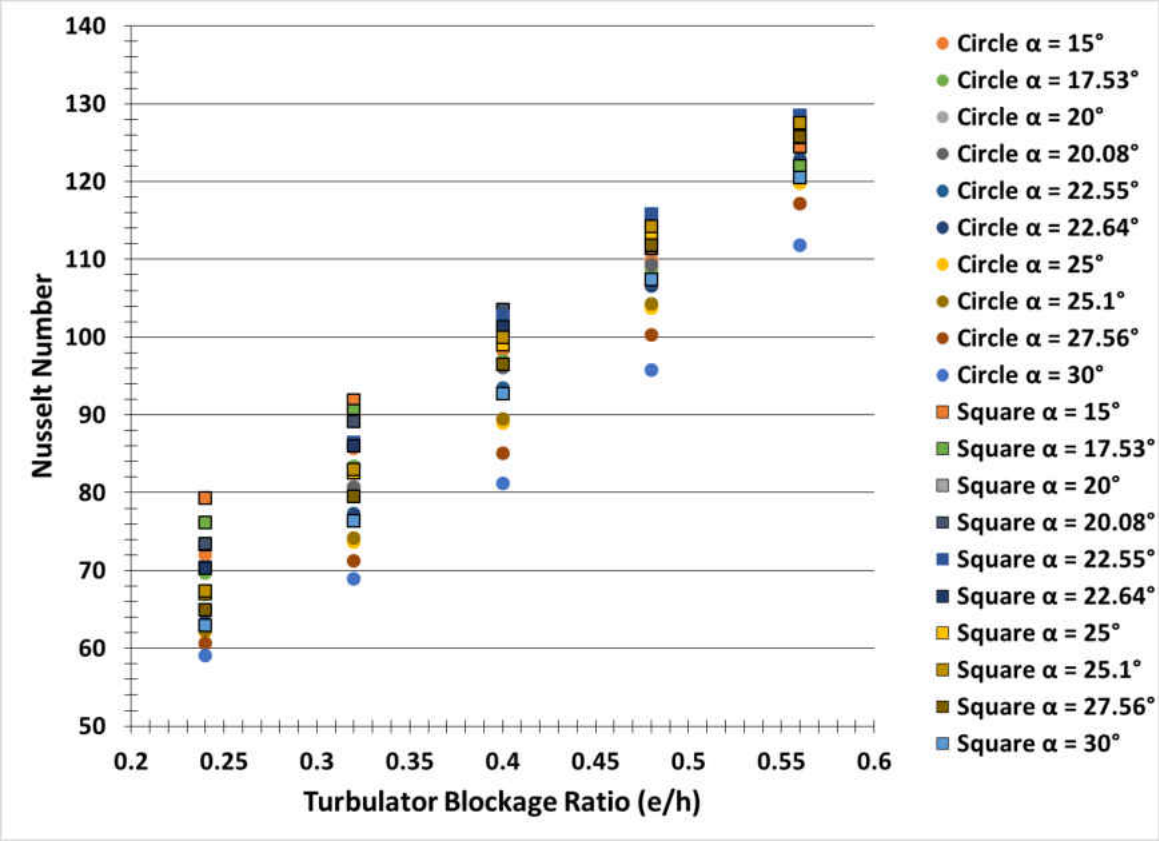

Figure 5.8: Nusselt Number vs. Blockage Ratio

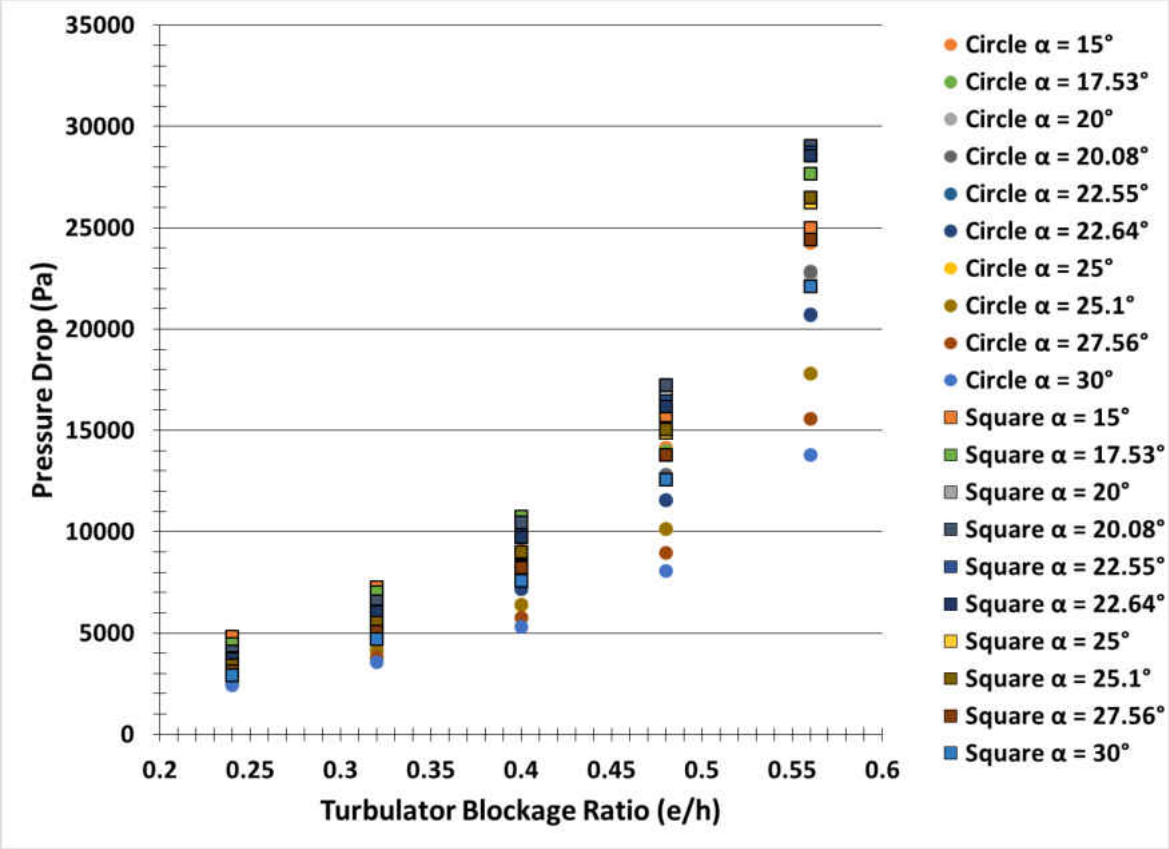

Figure 5.9: Pressure Drop vs. Blockage Ratio

CHAPTER 6: ANNULAR IMPINGEMENT EXPERIMENTAL SETUP AND DATA REDUCTION

To test the effects of impingement flow within an annulus, two different inner pipes were used. These inner pipes had the same locations of where the impingement jets are around the circumference except the diameter of the impingement holes were different. The flow pattern is shown in Figure 6.1. Flow enters through an insert pipe and travels through the various impingement holes located around the circumference of the insert pipe and bottom of this pipe. The bottom of the insert pipe is also blocked off but does have impingement holes as well. The flow impinges and hits the heated outer pipe and then exits through an outlet bore hole located a distance down the outer pipe.

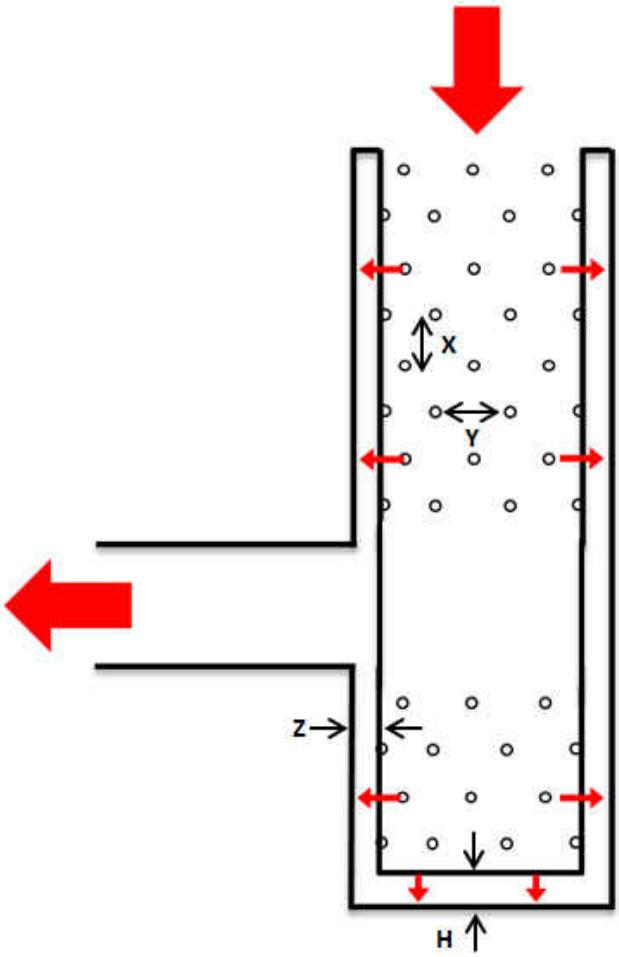

Figure 6.1: Impingement Flow Configuration (Cut Plane)

The insert is manufactured out of Rohacell RIMA 110 material with a thermal conductivity of (k = 0.0285W/mK) to closely simulate adiabatic conditions. Two inserts are experimentally tested with different X/Dj, Y/Dj, and Z/Dj. An annular diameter ratio of 0.92 was used for both geometries.

An experimental facility was used to capture the local and global heat transfer from the impingement onto a curved surface. To create a constant uniform heat flux around the annulus and end cap, three sections of heaters were used. Five heaters were used around the top half of the outer annulus, four heaters were located around the bottom half of the outer annulus and one

heater on the end cap. The heaters are individually controlled by six solid state relays and variacs to ensure equivalent heat flux. Relays have a capacity of up to 25 amps and 24-380 VAC. The variacs have a capacity of 20 amps and 120 VAC. Shunts of known resistance with uncertainty of less than one percent are placed between relays and heaters. These shunts are utilized to correctly measure the effective resistance of each heater once undergoing heating. A picture of this set-up is shown in Figure 6.2. The solid state relays are controlled by a 16 channel relay board equipped with 12 amps and up to 30V DC. Constant voltage is passed through solid state relays and deactivated by micro controller connected directly to a computer with Labview.

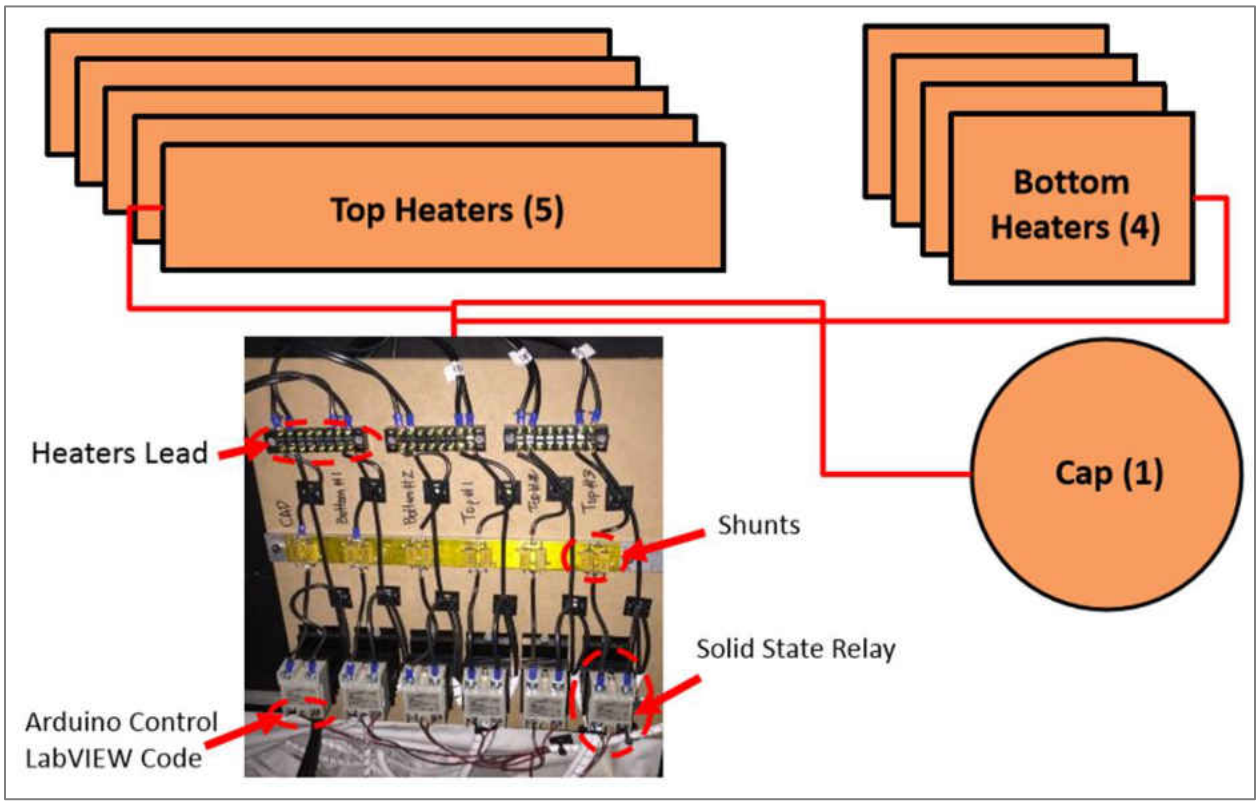

Figure 6.2: Heater Controller Configuration

The exhausted coolant flow is directed through an aluminum pipe with a length of 15 times the hydraulic diameter of the exit bored hole located at the pressure recovery zone of the acrylic pipe. Fluid moves through the pipe system, composed of schedule 40 PVC piping ranging

from three inches to six inches in diameter. Fluid reaches two three inch venturis where temperature and pressure across and upstream of the venturi is recorded. Venturi calibration curve was obtained using sonic nozzle configuration and is shown in Figure 6.3. For the both venturi configurations, ten times the hydraulic diameter piping upstream and five times downstream to ensure that flow was fully developed before reaching the venturi.

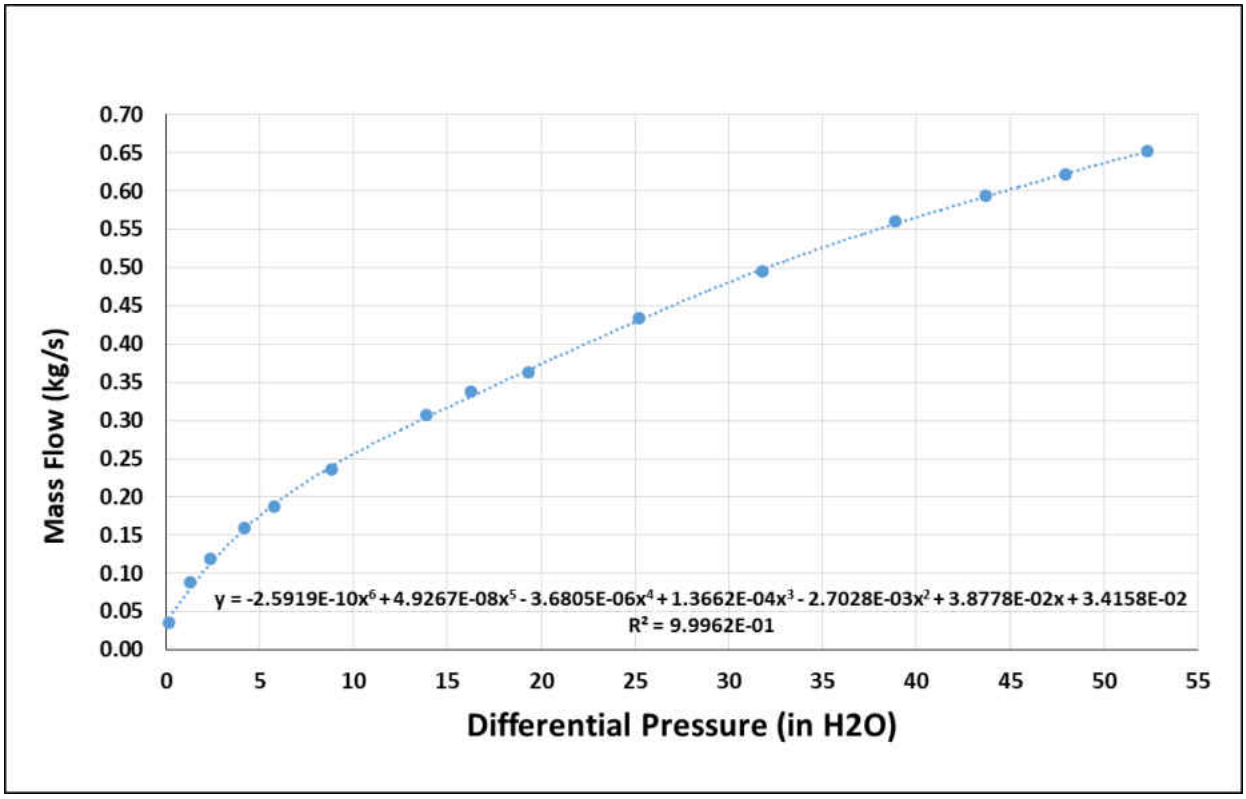

Figure 6.3: Venturi Calibration Curve

The experimental rig was designed to be under suction with an open circuit loop in order to utilize an Air Tech (250HP) blower at highest efficiency. The experimental mass flow rate is controlled by a gate valve located before the blower inlet. Substantial air bleeding was required to achieve the desired averaged jet Reynolds numbers. Air is exhausted to the outside of the building thus eliminating hot recirculating air inside the experimental room location. The Experimental rig is shown in Figure 6.4.

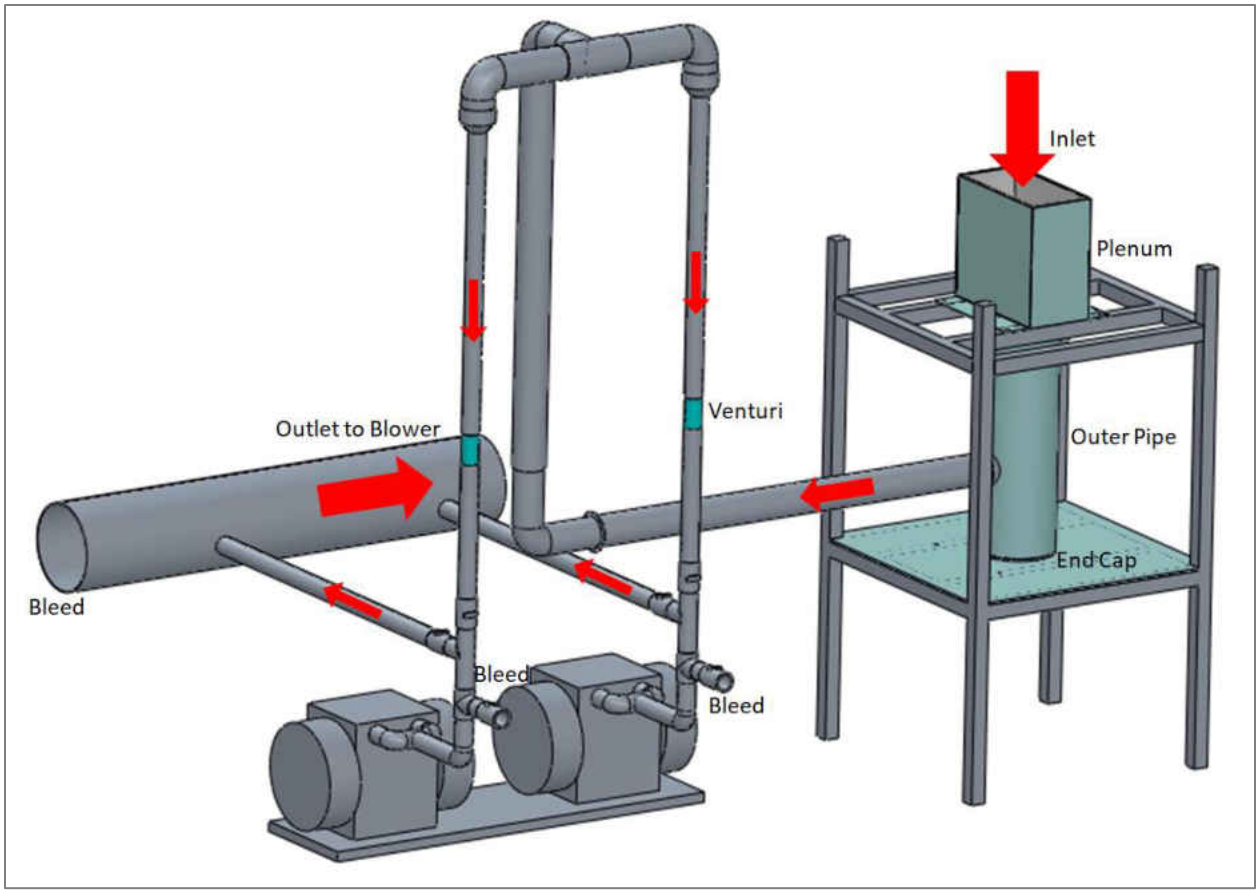

Figure 6.4: Experimental Rig Schematic

Two different geometric inserts were experimentally tested for three different averaged jet Reynolds numbers. For both inserts, the upper portion and pressure recovery zone are the same configuration, however for the bottom of the insert, Geometry B (GB) has four circumferential jets versus three in Geometry A (GA). The extra row of jets increases the total length of the insert, thus making the cavity between the insert end and acrylic end cap smaller. The insert bottom cap contains eight total jets for GA, and 23 for GB. The four circumferential jets at the edge of the insert end cap for both geometries are oriented at a 45º impinging angle. Jet configuration and insert parameters can be found in Table 6.1. The total quantity of jets and the spacing (H/Dj) between the insert end cap and annular tube cap can also be found. Both geometries GA and GB are tested for multiple Reynolds numbers ranging from 16,000 to 33,000.

The averaged hydraulic diameter for each geometric case is calculated and used as the Reynolds number length scale.

Table 6.1: Insert Geometric Parameters

Geometry	X/D_j	Y/D_j	Z/D_j	H/D_j	Jet #
A	8.4	8.4	1.8	7.4	112
B	9.2	9.2	1.9	2.9	135

Temperature Sensitive Paint (TSP) was applied to a 180º section of the acrylic pipe and end cap where polymide heaters were exerted to the testing surface via pressure sensitive adhesive. Polymide heaters cover the entire inner surface of the pipe and end cap. Figure 6.5 shows where the TSP and heaters were applied. The black pin stripping on the outer pipe was used for post processing the images.

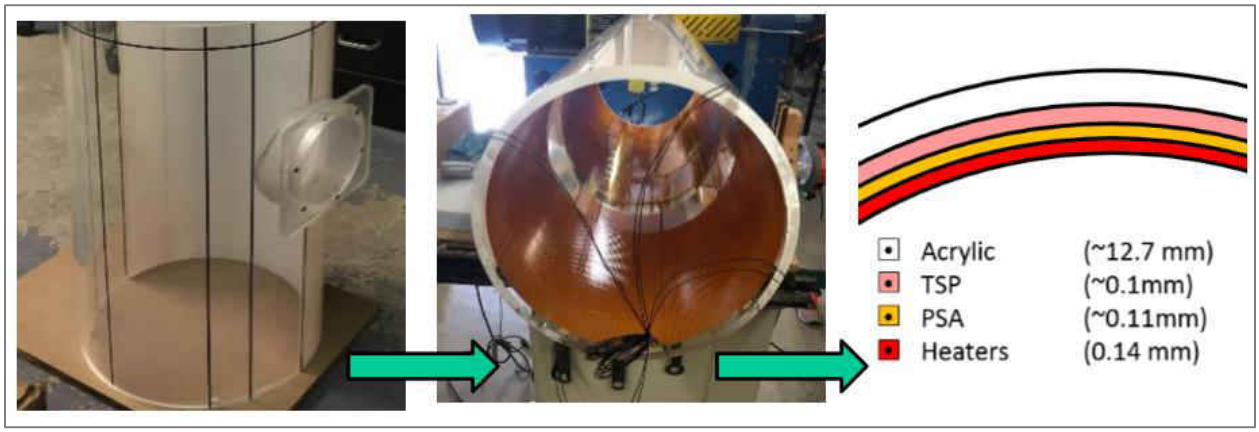

Figure 6.5: TSP and Heater Application Process

Resistance versus temperature curve was obtained before applying the heaters to the experimental surfaces. The heaters are sandwiched between two sheets of two inch thick Rohacell where thermocouples are placed within the polymide heaters to capture temperature. The applied voltage and heater resistance parameters are simultaneously recorded. From the data

obtained, calibration curves for each type of heater were constructed for data reduction purposes when post-processing experimental results which can be seen in Figure 6.6. Resistance ratio vs. temperature plots were also obtained and were compared to data from Ji-Song Han which is shown in Figure 6.7. From the calibration curves, the heat flux value being applied to the inner surface of the pipe can also be determined during the experimental process.

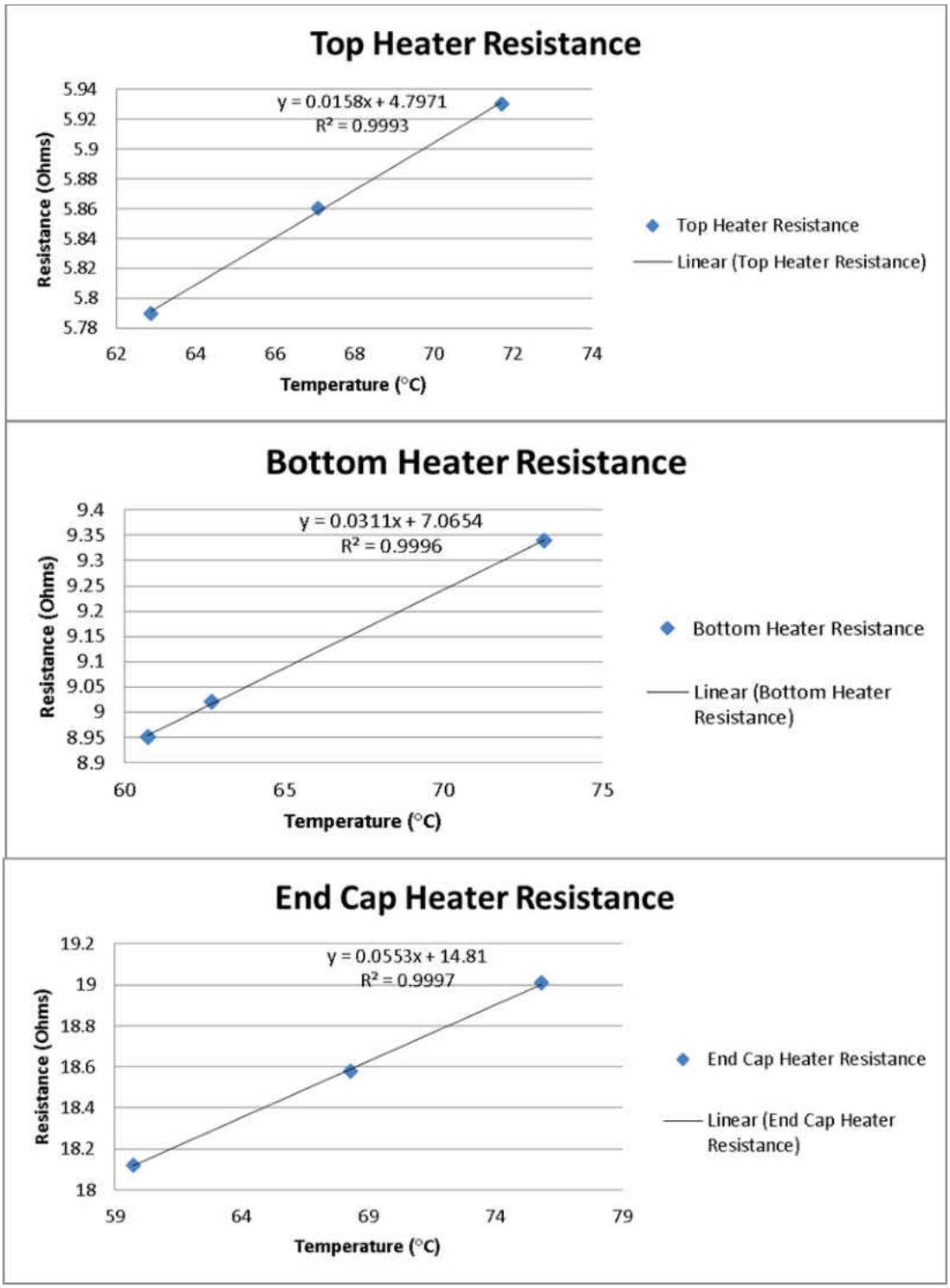

Figure 6.6: Calibration Curves for Heaters

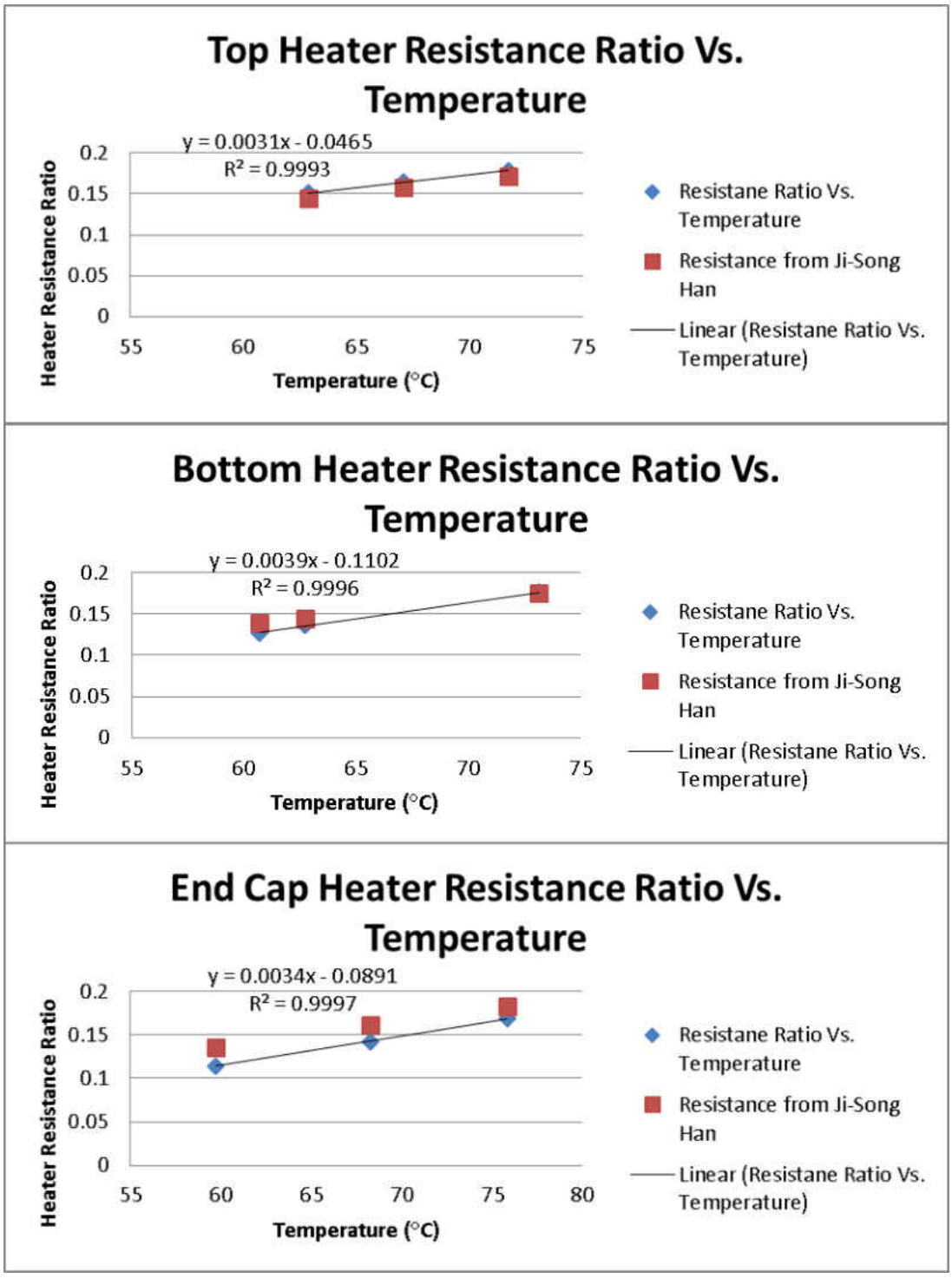

Figure 6.7: Heater Resistance Ratio vs. Temperature Plots

Prior to application, a calibration curve for the TSP is obtained from a separate test section in an enclosed vacuumed chamber, shown in Figure 6.8. A copper coupon embedded

with a US sensor of 50K Ohm thermistor with a resolution of ±0.05ºC is painted with TSP. The coupon undergoes is heated until it reaches a desired temperature by applying voltage to an adhered heater. A total of 8 sequential images are taken over a range of 25ºC to 85ºC with an Andor Zylas CMOS camera. Image intensities are normalized by the ratio of heated to unheated (reference) intensity, reducing to a TSP calibration curve for Intensity Ratio versus Temperature. A schematic of this set-up is shown in Figure 6.9. Detailed information about TSP process can be found in Liu [45].

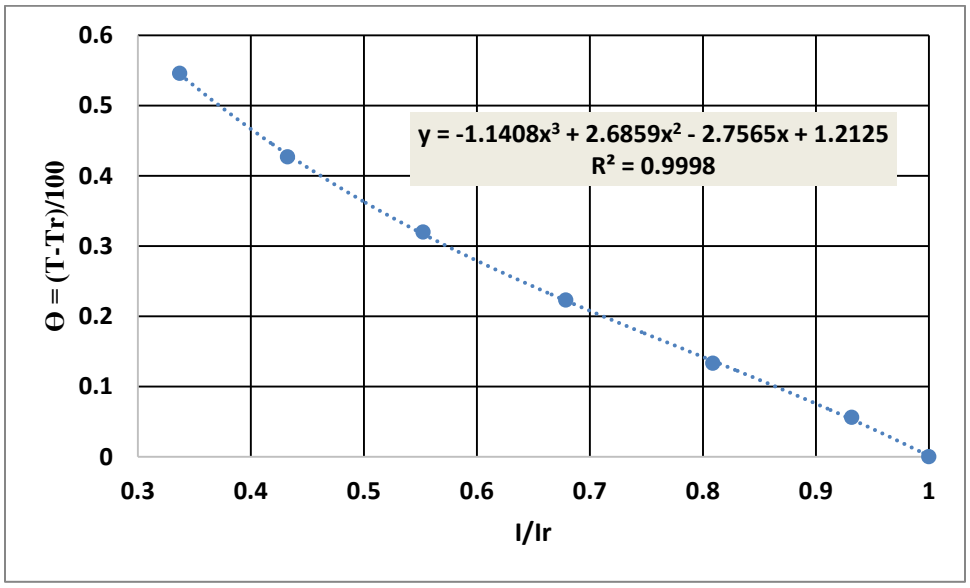

Figure 6.8: TSP Calibration Curve

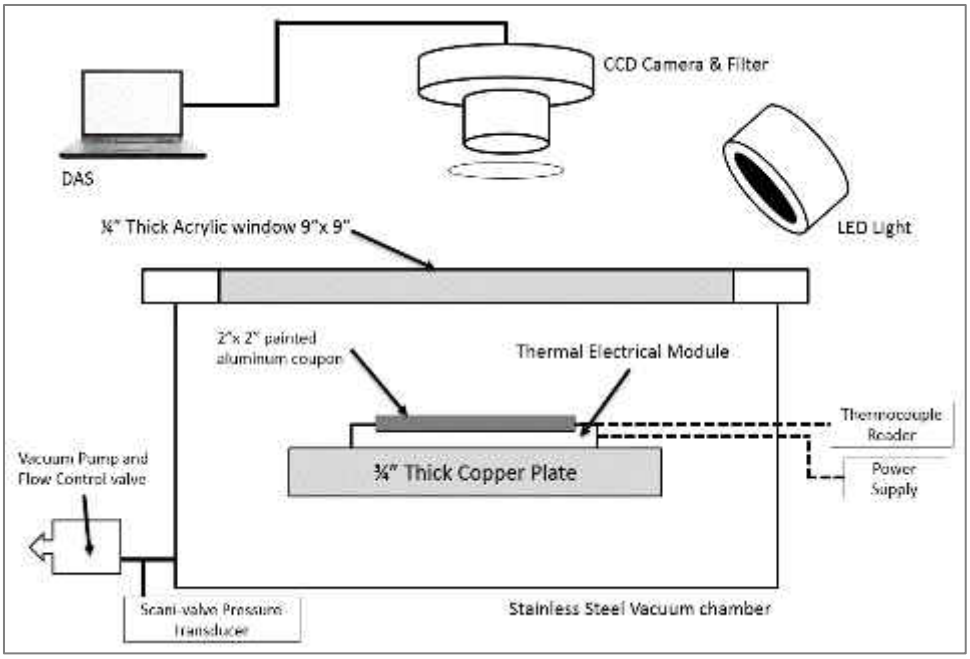

Figure 6.9: TSP Calibration Schematic

The experimental rig is completely enclosed in a box to eliminate any ambient light noise. During an experimental run, two sets of images are taken covering *a* and *b* positions with a total of three Andor Zylas sCMOS cameras with a resolution of 2560 by 2160 pixels. The first set of images are categorized as reference (cold) images where air is impinging into the surface with no heat flux being applied. A set of images are taken at position *a*, then cameras are traversed into position *b* where another set images are taken. Then, the polymide heaters are activated to the desired heat flux. Once steady state conditions are achieved, another set of images are taken at position *b* and categorized as steady-state (hot) images. The cameras are traversed into position *a* where the steady-state (hot) images procedure is performed again, which is shown in Figure 6.10. The set of images at the end cap of the facility is performed twice for redundancy and comparison.

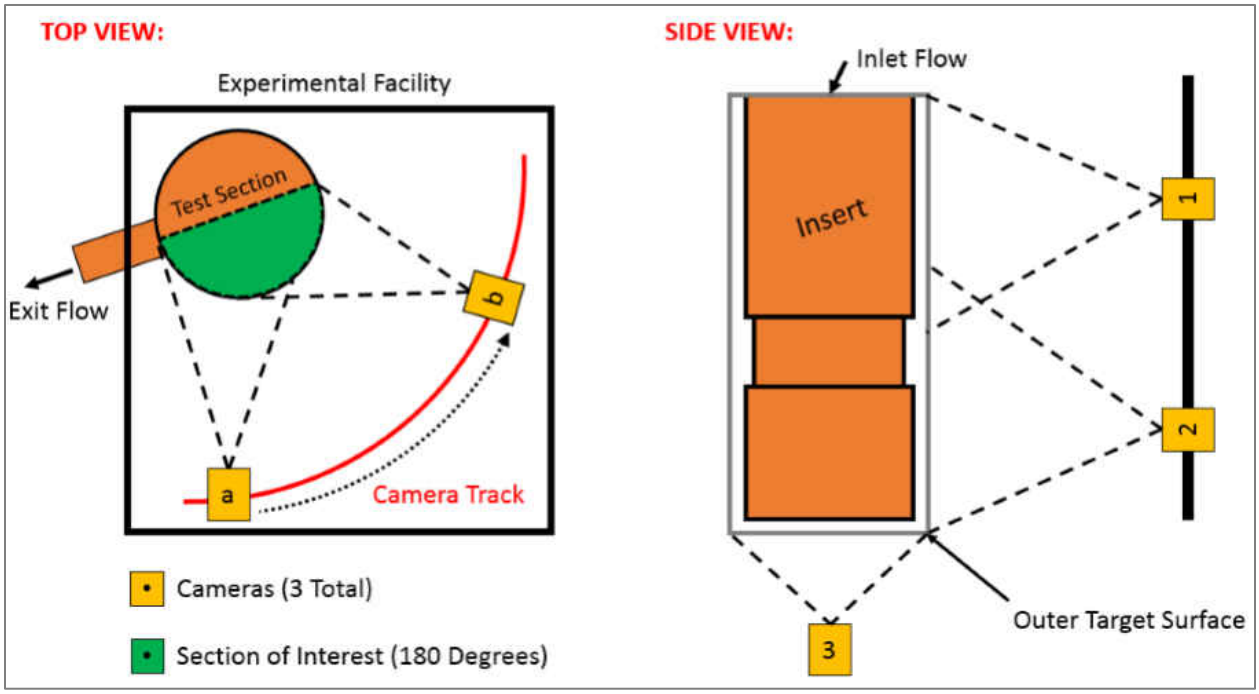

Figure 6.10: Experimental Rig Camera Positions

Each set is composed of eight images that are processed using an in-house developed Matlab code containing the TSP calibration mentioned above. A schematic of how the hot and cold pictures are post processed into heat transfer values is shown in Figure 6.11. Temperature and pressure measurements are obtained for the inlet of the conditioned plenum as well as at a distance of four times the hydraulic diameter of the exit bore flange. The values are utilized for experimental data reduction, and as boundary conditions for numerical simulations comparisons.

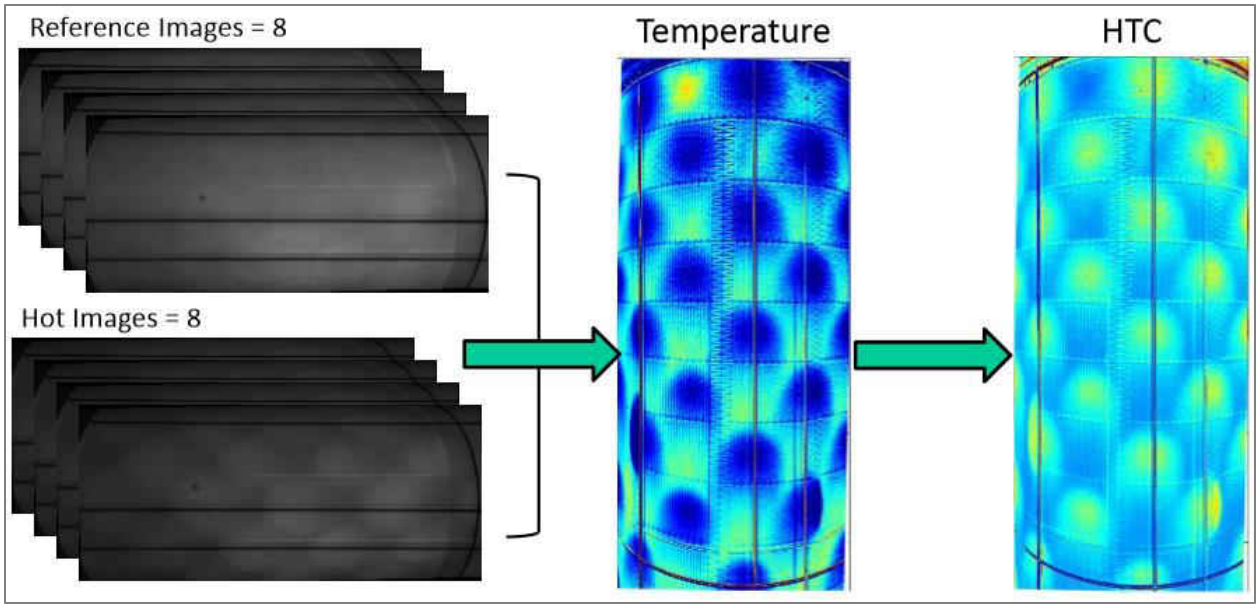

Figure 6.11: Schematic of Heat Transfer Data Reduction

A heat leakage test was performed on the experimental facility to quantify the amount of heat loss due to conduction through the acrylic outer tube wall. To quantify the amount of heat loss due to conduction, the annular gap was completely filled with fiberglass insulation along with thermocouples on the heaters surface and backside of the outer wall of the acrylic pipe. Multiple heat inputs were applied and the thermocouples temperatures across the surface were recorded. From the obtained data, a heat loss curve versus temperature difference was constructed shown in Equation 6.1.

$$q"_{cond} = 4.61[T_w(x,y) - T_b] \tag{6.1}$$

For heat loss due to radiation, fiberglass was removed and the facility was completely enclosed eliminating any possibility of natural convection. Similar test to conduction was performed and radiation loss as a function of temperature difference across the surface function was derived, shown in Equation 6.2. To estimate circumferential conduction a finite difference

method approach was used. The variation on the Nusselt number was less than one percent, thus the results presented here neglect the circumferential conduction effect.

$$q"_{rad} = 0.87[T_w(x,y)^4 - T_{surf}^4] \tag{6.2}$$

The heat flux generated on the inner wall of the acrylic pipe and endcap is produced by the resistance heating of the polymide heaters. The following equations were utilized to calculate the amount of heat produced.

$$q"_{gen} = \sum \frac{I^2 R}{A_h} \tag{6.3}$$

Since the heaters at the bottom, top and endcap surfaces of the acrylic test section have different total areas, the following resistances were found for the top (R_t), bottom (R_b), and endcap (R_c) heaters, respectfully, as a function of temperature.

$$R_t = 0.0158(T) + 4.7971 \tag{6.4}$$

$$R_b = 0.0311(T) + 7.0654 \tag{6.5}$$

$$R_c = 0.0553(T) + 14.810 \tag{6.6}$$

Using the formulation obtained above for radiation and conduction losses, the effective heat flux can be determined. After taking in consideration the impingement cooling mechanism the heat transfer coefficient can be found. Nusselt number is calculated using the averaged hydraulic diameter of all the impinging jets.

$$q"_{eff} = q"_{gen} - q"_{cond} - q"_{rad} \tag{6.7}$$

$$h = \frac{q"_{eff}}{T(x,y) - T_b} \tag{6.8}$$

$$Nu = \frac{hD_j}{k} \tag{6.9}$$

Pressure ratio from inlet plenum to outlet exit bore was calculated from experimental results and compared to computational fluid dynamics (CFD) numerical simulations.

A Nikon wide angle 10-24 mm lenses was used to capture each set of images except at the end cap region. A wide angle correction code was used to transform the image plane. The image was then used to transform the annular curved surface into flat. Images were passed through an in house code with the data reduction techniques. The heat transfer coefficient was obtained and averaged in the circumferential direction; the (X/Dj) is referenced in the stream-wise direction. The (X/Dj) origin is located at the top edge of the impingement insert.

CHAPTER 7: ANNULAR IMPINGEMENT NUMERICAL SETUP

Experimental results were compared with CFD for validation. StarCCM+ was the numerical software chosen. For an exact comparison between CFD and experiment, boundary conditions were supplied directly from experimental results. However physical simplifications were made in order to reduce CFD computational time. Symmetry plane was claimed at the center of the experimental facility. A stagnation inlet boundary condition was applied at the inlet of the plenum where temperature and ambient pressure matched with experimental cases. The insert walls were considered no slip, smooth adiabatic walls. A no slip, constant uniform heat flux boundary condition was imposed on the inner acrylic tube wall and endcap. These boundary conditions can be seen in Figure 7.1. Pressure outlet condition was defined with a target mass flow rate in order to achieve the experimental averaged jet Reynolds numbers ranging from (Rej = 16,000 to 33,000).

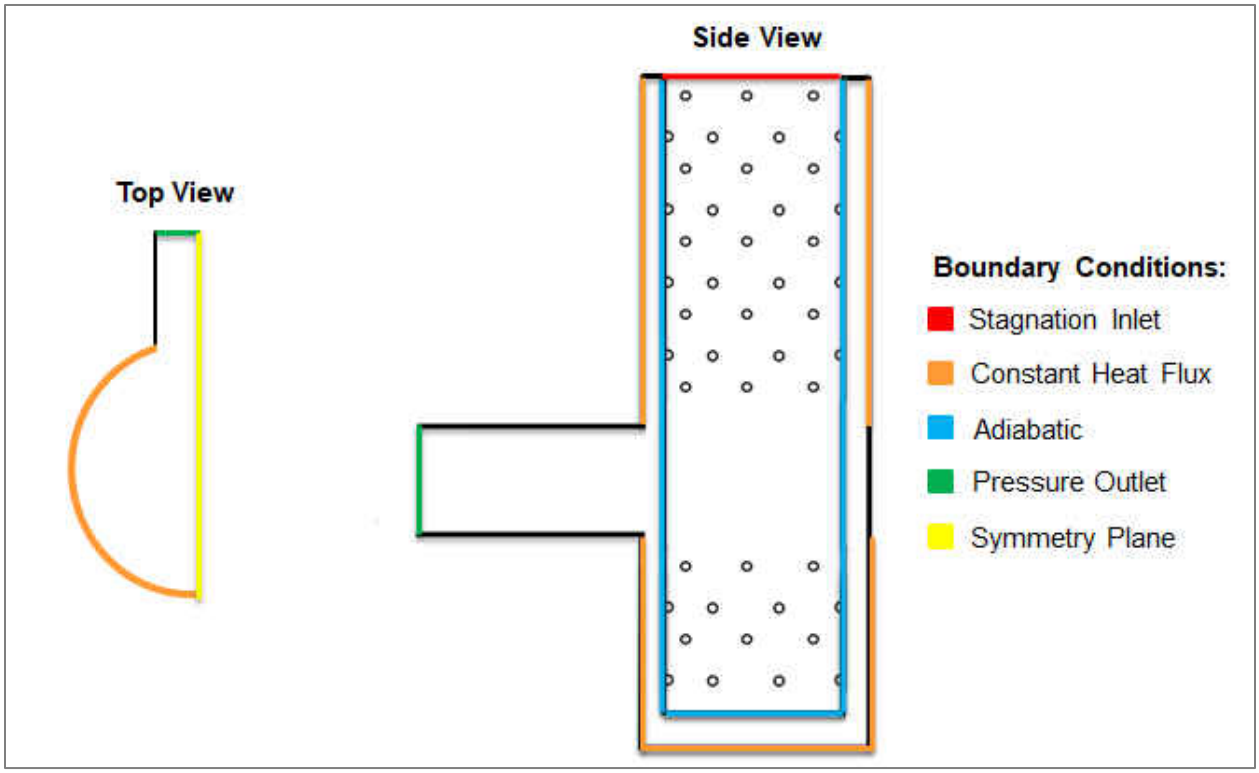

Figure 7.1: Numerical Boundary Conditions

The k-ε turbulence derivative model υ^2-f was utilized to model the jet impingement physics. The model is known to accurately capture near-wall turbulence effects at a significantly less computational cost in comparison to Direct Numerical Simulations (DNS) and Large Eddy Simulation (LES) methods. The υ2-f is a four equation turbulence model developed by Durbin et al. [46] and further analyzed by Zuckerman and Lior [36]. The model solves the two original equations of turbulence kinetic energy (k), and dissipation rate (ε) as well as modified velocity variance scale (υ^2), and elliptic relaxation function (f). The model is able to integrate all the way to the wall, making it ideal for capturing turbulent wall effects due to the tangential velocity fluctuations and non-local effects. Fluid Temperature and Segregated Flow models were solved using a second order up wind scheme. Residuals for momentum, temperature, heat transfer

coefficient, pressure, and turbulence statistics were closely monitored for convergence requirements.

A mesh sensitivity analysis was completed in order to understand if numerical solutions were mesh independent. After solution convergence was reached, an additional 2500 iteration values were averaged for heat transfer coefficient and used to calculate Nusselt number, using an averaged jet diameter as length scale for each geometry. Total Nusselt number for the annular wall, temperature, and pressure at the outlet of the domain were used as investigation parameters for sensitivity analysis. The numerical simulation mesh utilized on this study was also based on the ability of the cell count to deliver a (y+) as close to unity as possible. Figure 7.2 shows the wall Y+ for each geometries annular section. With a maximum value less than one, flow in the viscous sublayer will be predicted accurately. Figure 7.3 shows the mesh grid independence for the cases analyzed. It was concluded that a mesh count of 13 Million cells and 12 Million cells were sufficient for GA and GB, respectively.

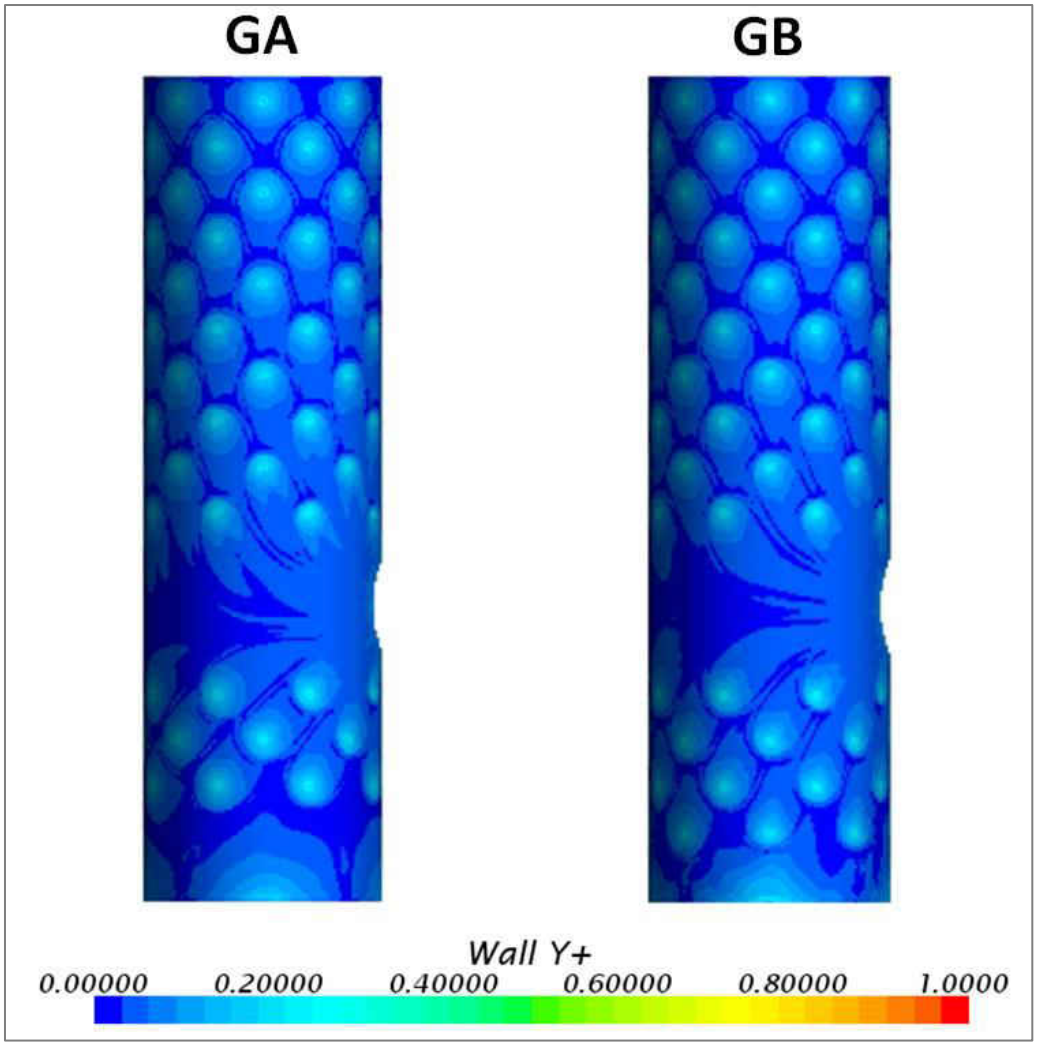

Figure 7.2: Outer Annulus Wall Y+ for Geometry A and B

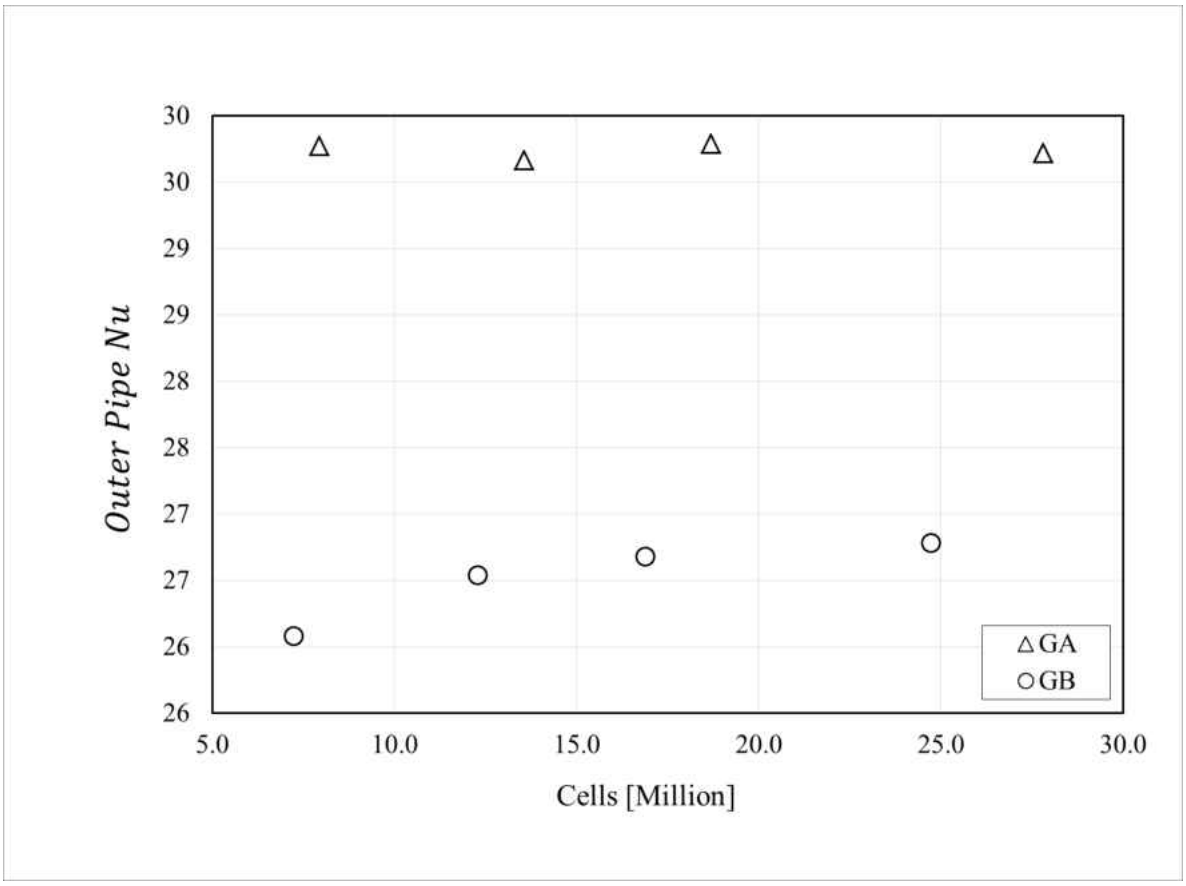

Figure 7.3: Mesh Sensitivity Analysis for Geometry A and B

CHAPTER 8: ANNULAR IMPINGEMENT RESULTS

The experimental results for the first ten jets are compared to forced convection for a concentric annular tube. For comparison, the improved Gnielinski correlation for turbulent flow in concentric annular ducts was used. The correlation predicts a Nusselt number value as function of annular ratio, Reynolds number, and Prandlt number. Using the experimental mass flow rate and annular gap, a total heat rate ($\dot{Q}$) was calculated for forced convection within a concentric annular duct where the inner tube was insulated and the outer tube had an imposed constant heat flux condition. Using the log mean temperature difference (LMTD) analysis, the total heat rate was calculated for the case where no impingement was present. The total heat transfer rate was obtained experimentally, for both geometries GA and GB. The heat rate for the plain annular case was utilized as baseline for both experimental cases. As it can be observed from Figure 8.1, utilizing staggered jet impingement design resulted in an improvement in heat rate effectiveness. Compared to the convectional convection cooling mechanism, jet impingement produced a higher heat removal effectiveness for the same given mass flow rate. The behavior can be attributed to jet impingement constant renewal of coolant flow impacting the heated surface. For impingement mechanism the boundary layer is much thinner in comparison to convection where the boundary layer increases until it completely fills the annular gap.

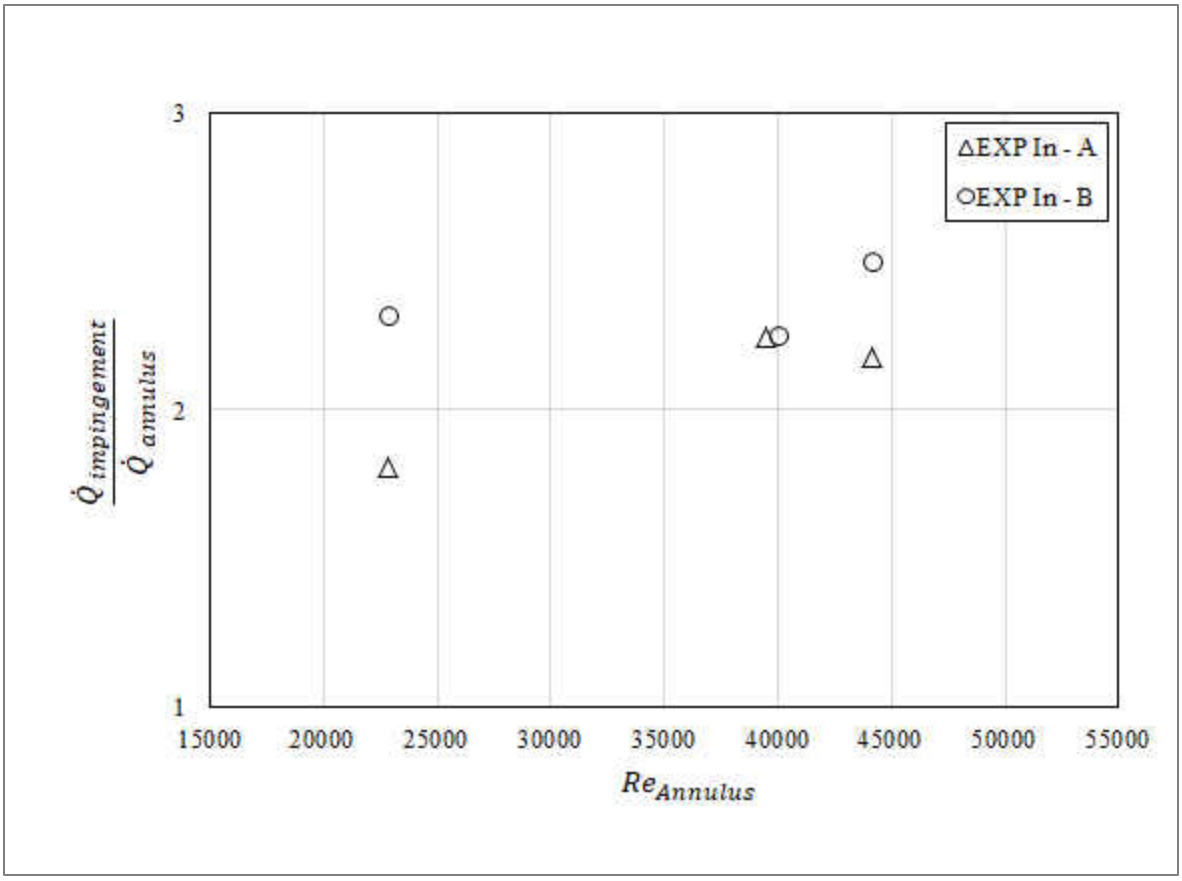

Figure 8.1: Enhancement Ratio for both Experimental Geometries Compared to CFD for Convection Cooling

The overall heat transfer behavior differs between the baseline and impingement geometry. For the forced convection concentric annular tube, the heat transfer effectiveness decreases as the fluid travels from the inlet to the outlet for the same given length. The convective mechanism creates uneven cooling distribution along the length of the annular tube which in term can affect the overall life expectancy of the material, for example cooling methods for industrial application purposes. To reach higher heat transfer, significant mass flow rate must be utilized incurring a larger pressure penalty. In the case of jet impingement, a uniform heat transfer distribution can be obtained at a lower mass flow rate and pressure penalty. However the

impingement case suffers from the possibility of jet degradation incurred from the cross-flow of the interacting jets.

A figure 8.2 show that for the same annular ratio, as the mass flow rate is increased the overall surface averaged Nusselt increases. This pattern follows typical impingement studies performed by [27] in which for a given (Z/Dj), as the jet Reynolds number is increased the Nusselt number monotonically increases. Numerical results for each averaged jet Reynolds number was compared with experimental results, with a 12% uncertainty bar. The experimental uncertainty was calculated on a 95% confidence interval using the methods outline in Figliola and Beasly [47].

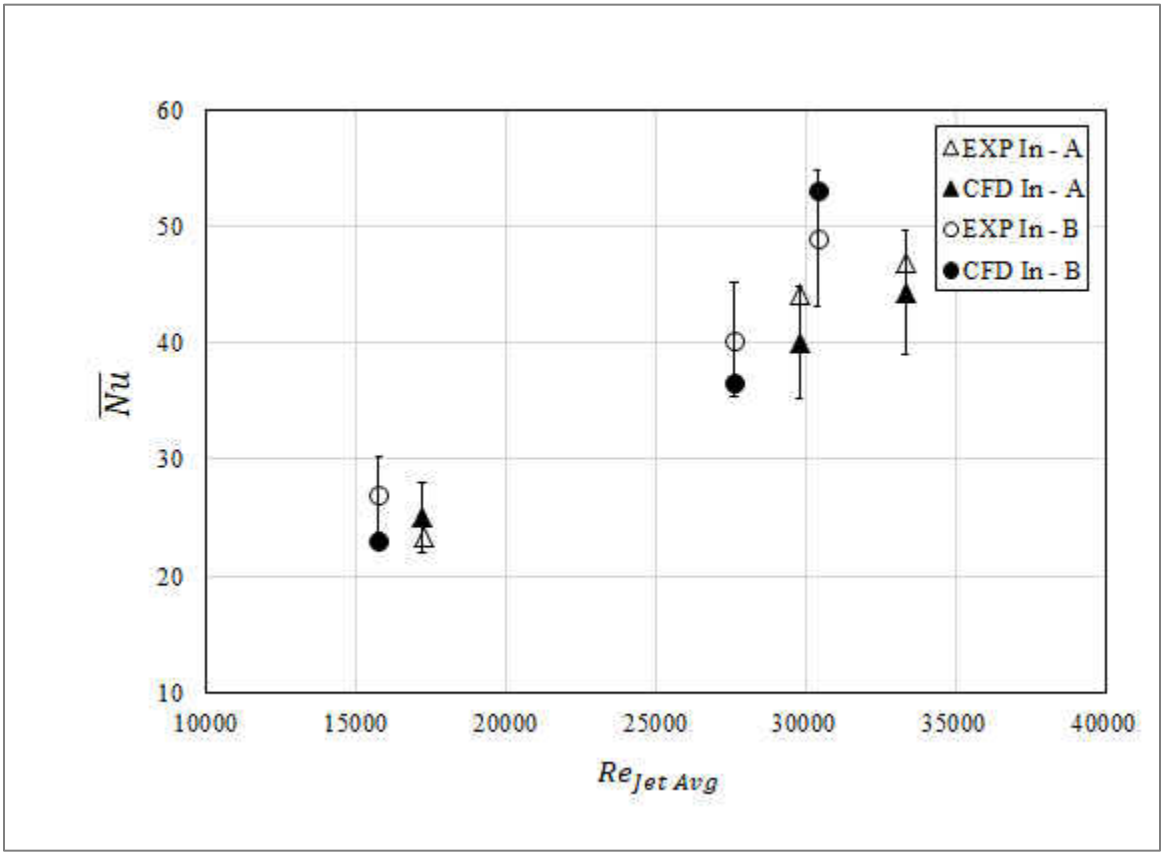

Figure 8.2: Surface Averaged Nusselt Number for Staggered Jet Impingement Pattern for Concentric Annular Tube with Heated Outer Annulus

Figure 8.3 and 8.4 contains the uncertainty diagrams for Nusselt number and Reynolds number, respectively. With all of the uncertainties accounted for, Table 8.1 lists the bias, precision and total percent values for the experimental uncertainty.

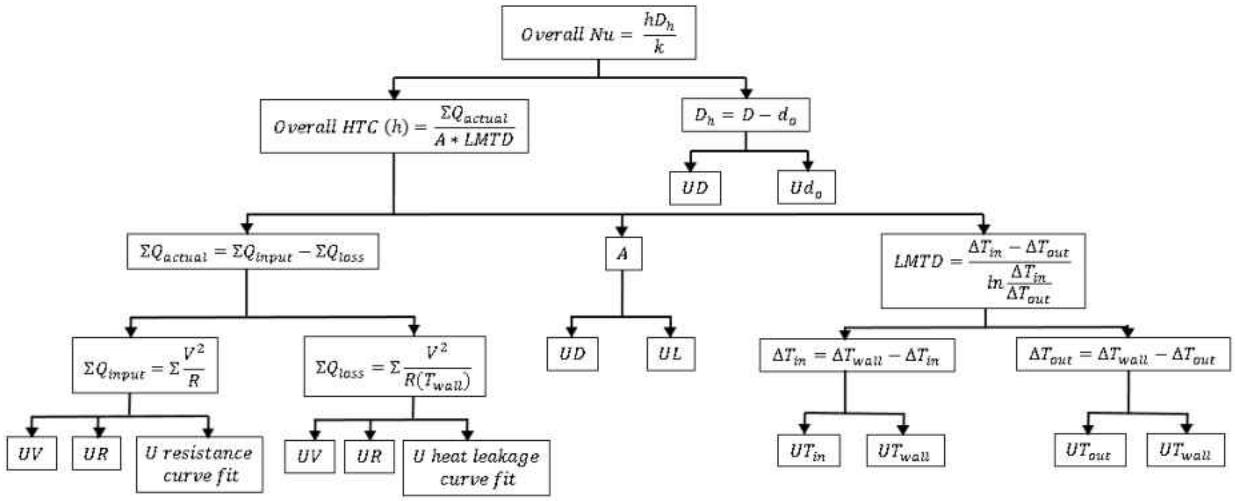

Figure 8.3: Nusselt Number Uncertainty Diagram

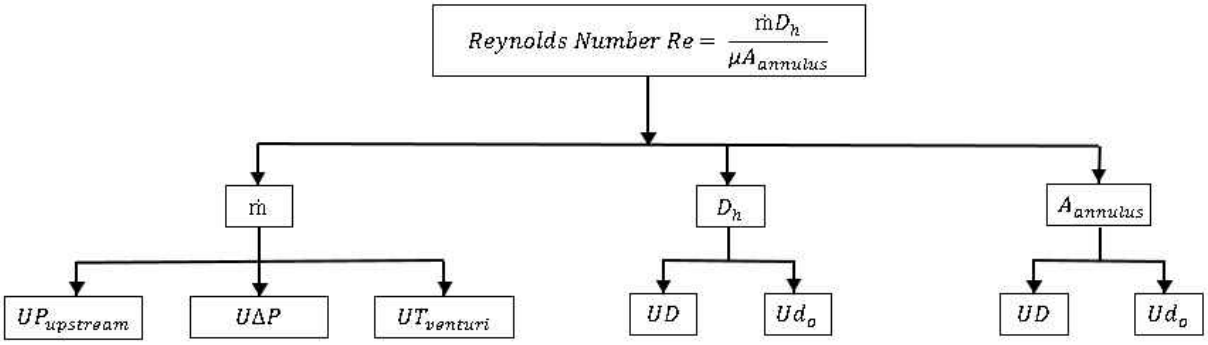

Figure 8.4: Reynolds Number Uncertainty Diagram

Table 8.1: Calculated Experimental Uncertainty

	Bias	Precision	Total
Nusselt Number	5.10%	4.18%	12.25%
Reynolds Number	0.50%	1.09%	1.20%

A predominant assumption for jet impingement problem found through literature is the utilization of a flat target surface to represent curved surface. Curvature possible effects on heat transfer is assumed negligible due to the radius of curvature of the target surface being significantly larger than the jet diameter. However, strong curvature and cross-flow effects can be found when analyzing the lateral surface average Nusselt number for the geometries presented here.

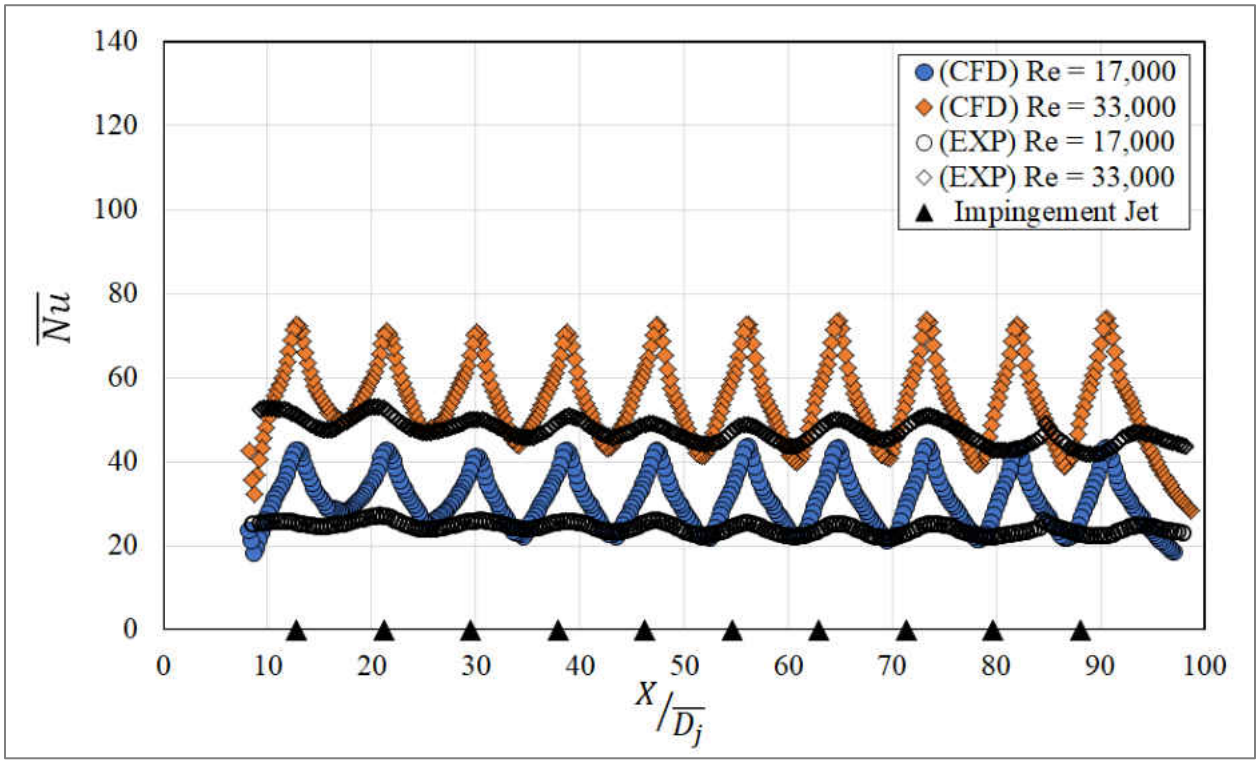

Figure 8.5: Lateral Surface Averaged Nusselt Number Comparison between CFD and Experimental Data for Geometry A

The lateral averaged Nusselt number was calculated by averaging experimental profiles in the streamwise direction with an uncertainty of 12%. Figure 8.5 and 8.6 show that stagnation point shift from the jet impingement location with a downward trend for Nusselt magnitude in the stream-wise direction for both experimental geometries. The surface averaged Nusselt value

decreases due to crossflow interaction between jets, where the boundary layer thickness grows and negatively impacts the heat transfer at the target surface.

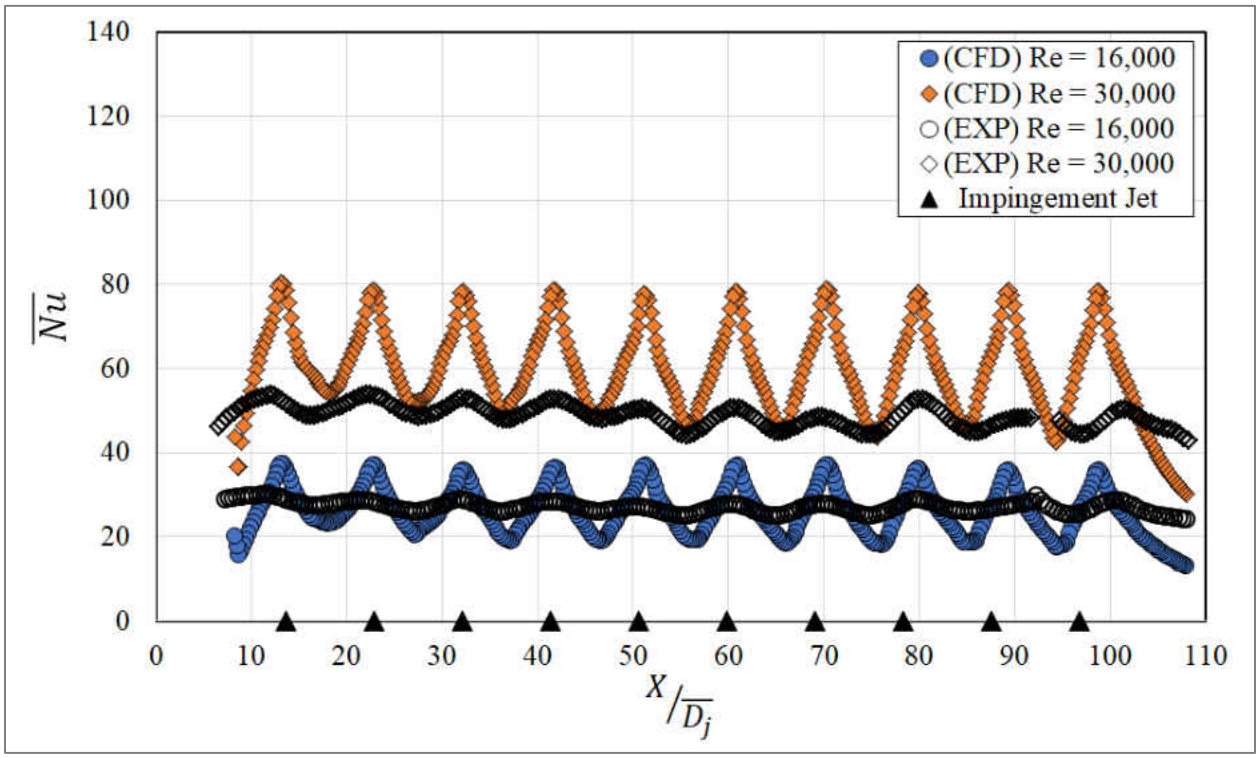

Figure 8.6: Lateral Surface Averaged Nusselt Number Comparison between CFD and Experimental Data for Geometry B

For Geometry A, the stagnation point shift becomes more evident after the sixth jet impinging location at the target surface. The cross-flow becomes stronger toward the last jet due to upstream flow accumulation. The jet to jet interaction decreases the impingement heat transfer effectiveness, and further exacerbated by the circumferential cross-flow. The cross-flow effect also enhances the convection heat transfer, but decreases the impingement cooling mechanism. From Figure 8.7, it can be observed that the heat transfer coefficient for jet impingement is higher than convection cooling due to cross-flow which is the same behavior was found by Florscheutz [48].

The air spent into the annular gap accumulates from top of the insert traveling to the pressure recovery zone where the outlet bore exit is located. The flow exhibits a rotational component as the fluid is siphoned out from the pressure recovery zone. This behavior increases the crossflow in the circumferential direction which diminishes the effectiveness of impingement heat transfer for the jets close to the pressure recovery region. At the same time convection heat transfer coefficient for the last two rows of jets increases thus maintaining desirable annular wall cooling.

Greater jet impingement degradation was observed for jets located closer to the outlet bore. As it can be seen in the lateral surface averaged comparison between experimental and numerical results, the last two jets rows suffer from heavy circumferential cross-flow behavior, shown in Figure 8.7. The surfaced averaged Nusselt number magnitude increased with an increase in jet averaged Reynolds number. From Figures 8.5 and 8.6, it was concluded that the lateral surface averaged profiles are independent to the magnitude of the Reynolds number which meet the same criteria found in literature. Furthermore, it was found that the CFD results were unable to properly predict the stagnation region after the eighth jet for both geometries; however, the jet impingement pattern was properly captured. The numerical results underestimate the stagnation shift in comparison to the experimental results.

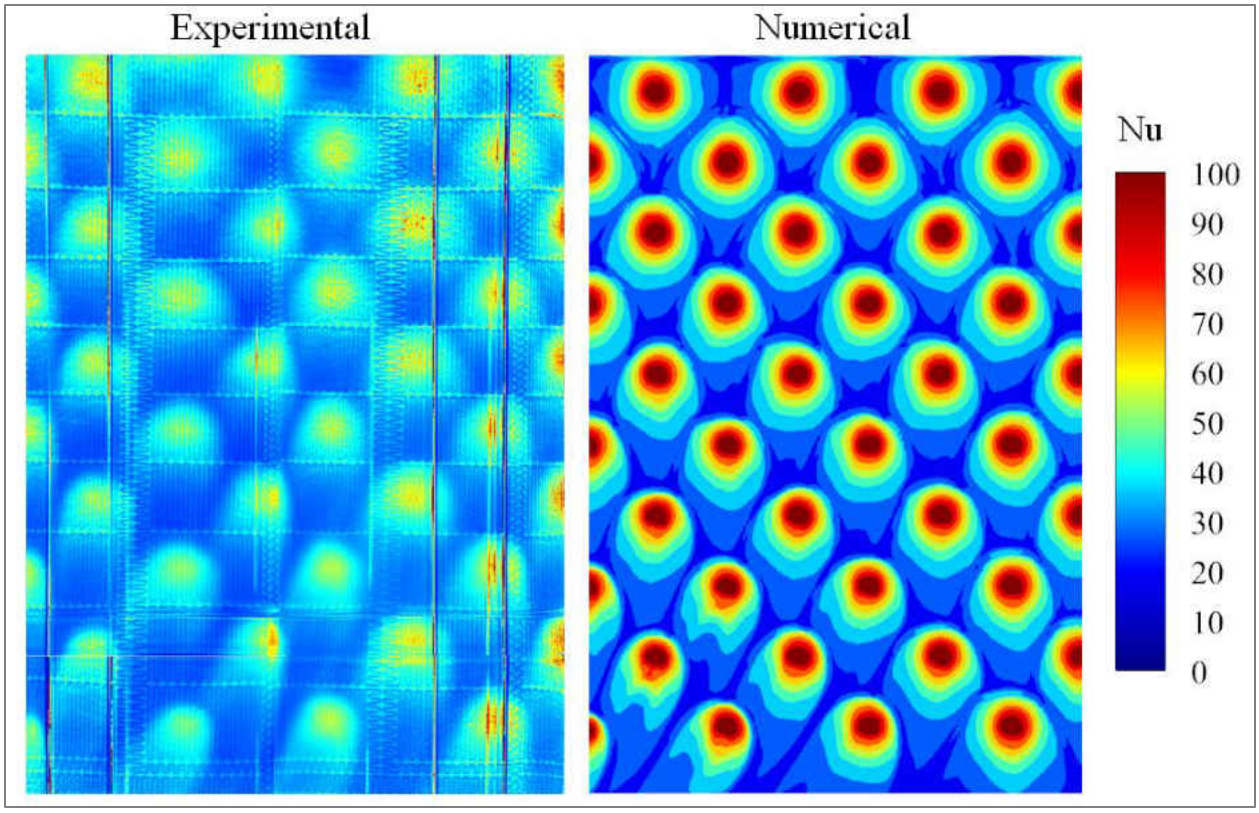

Figure 8.7: Nusselt Number Comparison between Experimental and Numerical Results for Geometry A and Re_{jet} = 30,000

The overall total Nusselt number was calculated by averaging the circumferential end cap and annular wall, the results are shown in Figure 8.8. The overall heat transfer rate for GB was found to be larger than GA. The pressure ratios for the experimental tests are shown in Figure 8.9. The inlet pressure and the pressure located downstream of the outlet bore pipe four times the hydraulic diameter of the outlet bore hole were used to determine the pressure ratios.

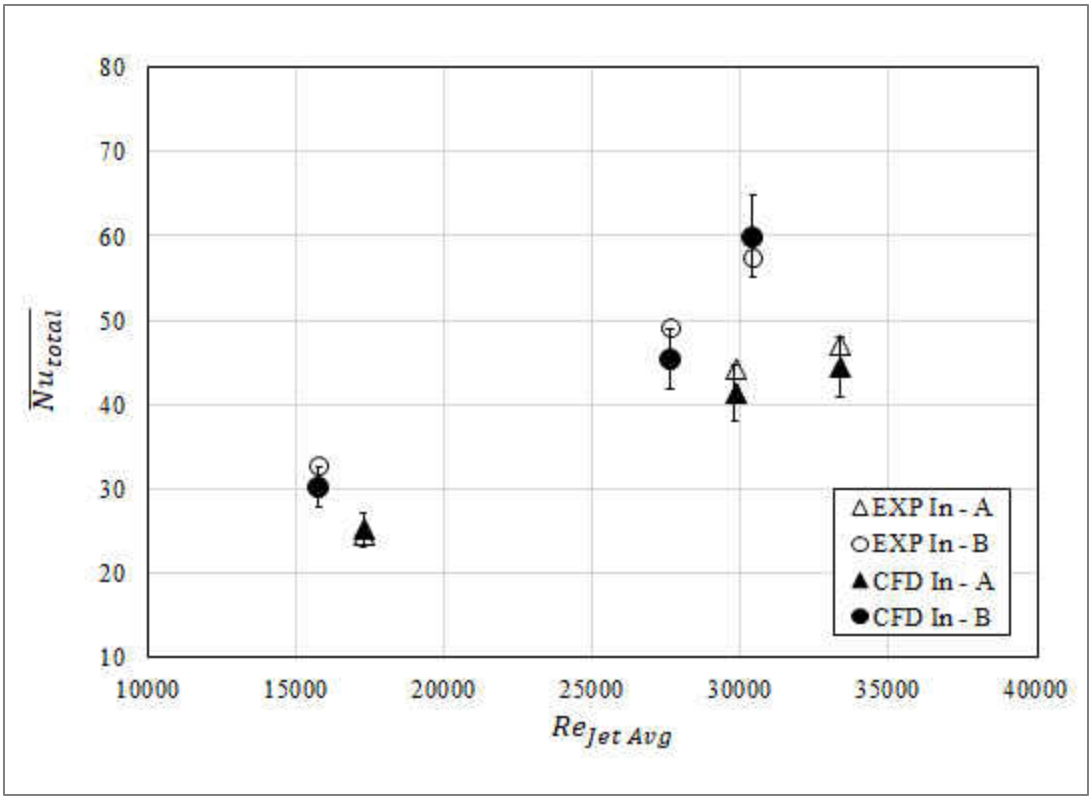

Figure 8.8: Experimental Total Nusselt Value (Annular Wall and Endcap) for Both Geometries

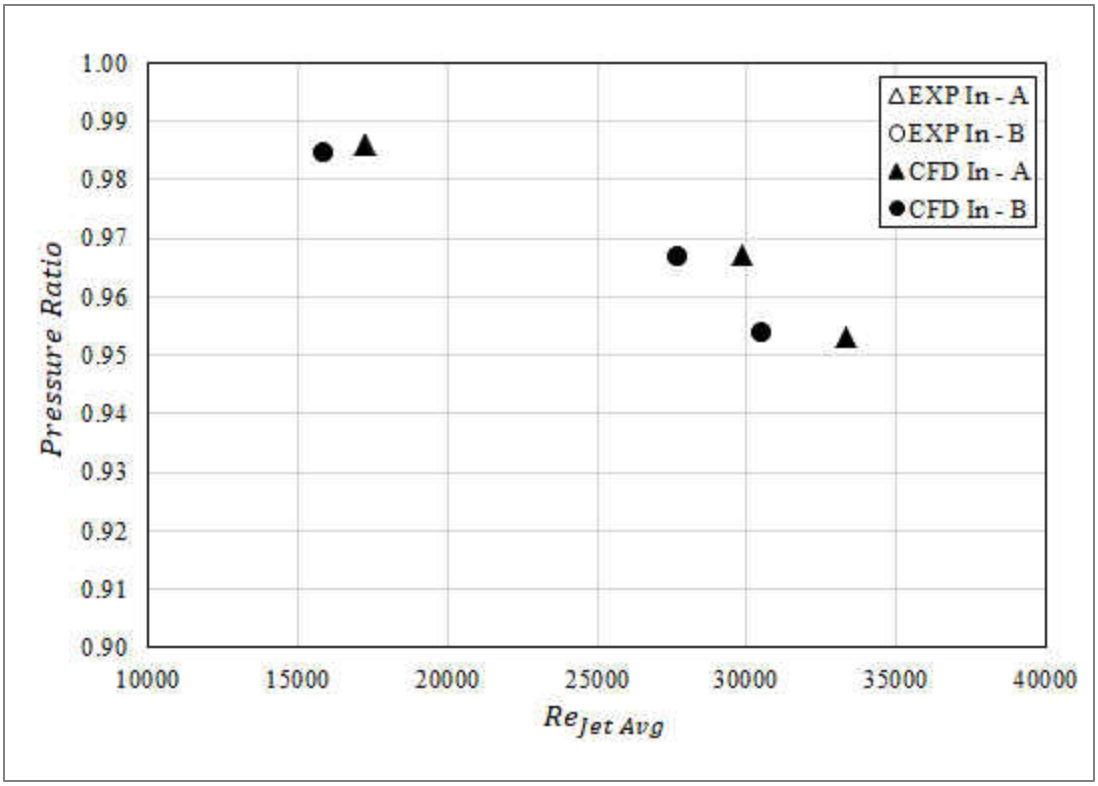

Figure 8.9: Experimental Pressure Ratio Obtained for Both Geometries

It can be concluded that even though there was more fluid spent into the annular gap for GA, it was not enough to compensate for the difference between annular wall and endcap. GB was able to deliver a better overall cooling of the outer surface than GA at almost the same pressure penalty. For heat removal in this type of heat exchanger, GB would yield the optimum design between both geometries. Pressure drop from inlet to outlet was accurately predicted from the numerical simulation model.

CHAPTER 9: CONCLUSION

Based on all of the simulations performed, turbulators promote higher heat transfer. It was found that as the blockage ratio increased and the pitch decreased, a higher Nusselt will result but an increase in pressure drop will also occur. With a higher blockage ratio, the turbulence from the helicoil turbulators will add a stronger "swirl" effect inside the annulus which promotes greater heat transfer. For the cases where the blockage ratio is 0.48 or greater, the tradeoff for Nusselt number and pressure drop is not as beneficial as the cases where the blockage ratios were smaller. The turbulator shape also impacted the heat transfer. The square turbulator promoted higher heat transfer compared to the circle turbulator but the pressure drop was significantly increased when the helix angle was greater than 20° and blockage ratio greater than 0.48.

Detailed experimental and numerical investigation was performed for two different geometric inserts composed of staggered impingement jet configuration. Both impingement inserts differ in X/Dj, S/Dj, Z/Dj, jet diameter, jet quantity, and H/Dj. Three different averaged jet Reynolds numbers were tested and used to validate CFD results. The first ten impingement jets and end cap were analyzed for both geometries. It was found that for both Geometry A and B, impingement jet effectiveness decreases for jets located close to the pressure recovery region. Stream-wise cross flow can be observed in the lateral surface average Nusselt number where significant jet stagnation shift can be noticed after the fifth row of jets for both geometries. The last two jets suffer from larger degradation due to circumferential and stream wise cross-flow.

To support experimental results CFD tool was used to compare surface averaged values from end cap and annular wall. The numerical simulation was carried using identical

experimental conditions for one to one comparison. CFD was able to accurately predict stagnation peaks for jet impingement, however failed to predict the circumferential cross-flow observed for the jets closer to the pressure recovery region. The circumferential cross-flow reduced the effectiveness of the impingement heat transfer but helped maintain large convective cooling for jet to jet regions. It was concluded that GB was able to remove more heat in comparison to GA with more impingement jets and same pressure penalty for a given mass flow rate. As a result for a heat exchanger design where an impingement insert is used to remove heat from the outer surface of the annular pipe, Geometry B design is recommended. Using jet impingement cooling mechanism will deliver a more uniform heat transfer distribution in comparison to forced convection cooling.

After investigation, heat exchangers that have internal turbulators or impingement jets can reduce part failure caused by higher thermal loads in industrial heat exchanger applications due to the great heat transfer capabilities on the heated outer wall of the annulus.

LIST OF REFERENCES

[1] Moreno, J., “Tapping the Underground” Delta-Montrose Electrical Association, Denver Post

[2] Dirker, J., and Meyer, J. P., Convective Heat Transfer Coefficients in Concentric Annuli, Heat Transfer Engineering, vol. 26, pp. 38–44, (2005)

[3] Gnielinski, V., Heat Transfer Coefficients for Turbulent Flow in Concentric Annular Ducts, Heat Transfer Engineering, 30:6, 431-436, (2009)

[4] Prandtl, L., Führer durch die Strömungslehre, Verlag Vieweg, Braunschweig, Germany, (1944)

[5] Petukhov, B. S., and Roizen, L. I., An Experimental Investigation of Heat Transfer in a Turbulent Flow of Gas in Tubes of Annular Section, High Temp., vol. 1, pp. 373–380, (1963)

[6] Kays, W. M., and E. Y. Leung. Heat transfer in annular passages—hydrodynamically developed turbulent flow with arbitrarily prescribed heat flux. International Journal of Heat and Mass Transfer 6.7 pp. 537-557, (1963)

[7] Promvonge,P., Eiamsa-ard, S., Heat transfer in a circular tube fitted with free-spacing snail entry and conical-nozzle turbulators. Heat and Mass Transfer 34, pp. 838-848, (2007)

[8] H. Iacovides M. Raisee, "Computation of flow and heat transfer in two-dimensional rib-roughened passages, using low-Reynolds-number turbulence models", International Journal of Numerical Methods for Heat & Fluid Flow, Vol. 11 Iss 2 pp. 138 – 155, (2001)

[9] Wang QW, Lin M, Zeng M, Tian L. Computational analysis of heat transfer and pressure drop performance for internally finned tubes with three different longitudinal wavy fins. Heat and Mass Transfer. 45(2):147-56, (2008)

[10] Yu, B., Tao, Q., Pressure drop and heat transfer characteristics of turbulent flow in annular tubes with internal wave-like longitudinal fins. Heat and Mass Transfer 40, pp. 643-651, (2004)

[11] Zamankhan, P., Heat transfer in counterflow heat exchangers with helicoil turbulators. Commun Nonlinear Sci Numer Simulat. 15, pp. 2894–2907, (2010)

[12] Agrawal, K., Kumar, A., Behabadi, M., Varma, H., Heat transfer augmentation by coiled wire inserts during forced convection condensation of R-22 inside horizontal tubes. Multiphase Flow 24, pp. 635-650, (1998)

[13] Lal, S. N. Experimental studies on condensation of refrigerant by turbulence promoter. Ph.D. thesis. Mech. And Ind. Eng Dept., University of Roorkee, Roorkee, India, (1992)

[14] Braga, C.V.M., Saboya, F.E.M., Turbulent heat transfer and pressure drop in smooth and finned annular ducts, Eighth International Heat Transfer Conference, San Francisco, California, vol. 6, pp. 2831-2836, (1986)

[15] Eiamsa-ard, S., Promvonge,P., Enhancement of heat transfer in a tube with regularly-spaced helical tape swirl generators. Solar Energy 78, pp. 483-494, (2005)

[16] Withers, J., Tube-Side Heat Transfer and Pressure Drop for Tubes Having Helical Internal Ridging with Turbulent/Transitional Flow of SinglePhase Fluid. Part 1. Single-Helix Ridging, Heat Transfer Engineering, 2:1, 48-58, (1980)

[17] Vicente, P., Garcia, A., Viedma, A., Heat transfer and pressure drop for low Reynolds turbulent flow in helically dimpled tubes. Heat and Mass Transfer vol. 45, pp. 543-553, (2002)

[18] Ozceyhan, V., Gunes, S., Buyukalaca, O., Altuntop, N., Heat transfer in a tube using circular cross sectional rings separated from wall. Applied Energy 85, pp. 988-1001, (2008)

[19] Taylor, C. Xia, J., Medwell, J., Morris, W., Numerical simulation of three dimensional turbulent flow and heat transfer within a multi-ribbed cylindrical duct. International Gas Turbine and Aeroengine Congress and Exposition Orlando, FL June 3-6, (1991)

[20] Akpinar, E., Evaluation of heat transfer and exergy loss in a concentric double pipe heat exchanger equipped with helical wires. Energy Conversion and Management 47, pp. 3473-3486, (2006)

[21] Rashkovan, A., Aharon, J., Katz, M., Ziskind, G., Optimization of rib-roughened annular gas-coolant channels. Nuclear Engineering and Design 240, pp. 344-351, (2010)

[22] Ashrafin, A., Andersson, H.I., Manhart, M., DNS of turbulent flow in a rod roughened channel. International Journal of Heat and Fluid Flow 25, 373-383, (2004)

[23] Thianpong, C., Eiamsa-ard, P, Wongcharee, K., Eiamsa-ard, S., Compound heat transfer enhancement of a dimpled tube with a twisted tape swirl generator. Heat and Mass Transfer 36, pp. 698-704, (2009)

[24] Maurer, M., Experimental and numerical investigations of convective cooling configurations for gas turbine combustors. Published by Stuttgart University, (2008)

[25] Moskvina, G., V.; Mostinskii, I., L.; Polezhaev, Yu., V.; Seliverstov, E., M.: Problems of and Prospects for the Investigation of the Thermal Conditions of Blades of High-

Temperature Gas Turbines (a Review Based on Presentations to the Third Russian National Conference on Heat Transfer). High Temperature, vol. 41, No. 5, pp. 708-723, (2003)

[26] L. W. Florschuetz, D. E. Metzger, D. I. Takeuchi, and R. A. Berry NASA Contractor Report 3217, (January 1980).

[27] L.W. Florschuetz, D.E. Metzger, and C.R. Truman NASA Contractor Report 3373, (January 1981).

[28] Lee, C.H., Lim, K.B., Lee, S.H., Yoon, Y.J., Sung, N.W., A study of the heat transfer characteristics of turbulent round jet impingement on an inclined concave surface using liquid crystal transient method. Experimental Thermal and Fluid Science, vol. 31, pp. 559-565, (2007).

[29] Yang, Geunyoung, Choi, Mansoo, Lee, J.S.. An experimental study of slot jet impingement cooling on concave surface: effects of nozzle configuration and curvature. Heat and Mass Transfer vol. 42, pp. 2199-2209, (1999).

[30] Kumar, A., BVSSS, P. Computational Investigations of Impingement Heat Transfer on an Effused Concave Surface. Asian International Conference on Fluid Machinery, (2011).

[31] Iacovides, H., Kounadis, D., Launder, B. Experimental study of the flow and thermal development of a row of cooling jets impinging on a rotating concave surface. Journal of Turbomachinery vol. 127, pp. 222-229, (2005).

[32] Cornaro, C., Fleischer, A., Goldstein, R. Flow visualization of a round jet impinging on cylindrical surfaces. Thermal and Fluid Sciences, vol. 20, pp. 66-78, (1999).

[33] Tawfek, A. Heat transfer studies of the oblique impingement of round jets upon a curved surface. Heat and Mass Transfer vol. 38, pp. 467-475, (2002).

[34] Kayansayan, N., Kucuka, S. Impingement cooling of a semi-cylindrical concave channel by confined slot-air-jet. Thermal and Fluid Science vol. 25, pp. 383-396, (2001).

[35] Cornaro, C., Fleischer, A., Rounds, M., Goldstein, R. Jet impingement cooling of a convex semi-cylindrical surface. Thermal and Fluid Science vol. 40, pp. 890-898, (2001).

[36] Zuckerman, N., Lior, N. Jet impingement heat transfer: physics, correlations, and numerical modeling. Advances in Heat Transfer vol. 39, pp. 565-631, (2006).

[37] Choi, M., Yoo, H., Yang, G., Lee, J., Sohn, D. Measurements of impingement jet flow and heat transfer on a semi-circular concave surface. Heat and Mass Transfer vol. 43, pp. 1811-1822, (2000).

[38] Craft, T., Iacovides, H., Mostafa, N. Modeling of three-dimensional jet array impingement and heat transfer on a concave surface. Heat and Fluid Flow vol. 29, pp. 687-702, (2008).

[39] Han, J., C.; Dutta, S., Internal Convection Heat Transfer and Cooling – An Experimental Approach (Part I+II). Published by von Karman Institute for Fluid Dynamics, Lecture Series 1995-05, (1995)

[40] Hossain, J., Curbelo, A., Garrett, C., Wang, W., Kapat, J., Thorpe, S., Maurer, M., Use of Rib Turbulators to Enhance Postimpingement Heat Transfer for Curved Surface. Journal of Engineering for Gas Turbines and Power 139(7), pp. 071901-17

[41] Momin. E.; Saine, J. S.; Solanki, S. C.: Heat Transfer and Friction in Solar Air Heater Duct with V-shaped Rib Roughness on Absorber Plate. Int. Journal of Heat and Mass Transfer, vol. 45, pp. 3383-3396, (2002)

[42] Al-Hadhrami, L.; Griffith, T.; Han, J. C.: Heat Transfer in Two-pass Rotating Rectangular Channels (AR=2) with Five Different Orientations of 45 deg V-shaped Rib Turbulators. ASME Journal of Heat Transfer, vol. 125, pp. 232-242, (2003)

[43] Wang QW, Lin M, Zeng M. Effect of blocked core-tube diameter on heat transfer performance of internally longitudinal finned tubes. Heat Transfer Eng 29(1):107–115, (2008)

[44] M. Peric. Flow simulation using control volumes of arbitrary polyhedral shape. In ERCOFTAC Bulletin, No. 62. M. Peri´c and S. Ferguson. The advantage of polyhedral meshes. http://www.cd-adapco.com/. (September 2004).

[45] Liu, T., Pressure-and Temperature-Sensitive Paints. Wiley Online Library. (2005).

[46] Durbin,P., Separated flow computations with the k-v^2 model. AIAA journal, 33(4), (1995).

[47] Figliola, R. S., and Beasley, D., Theory and design for mechanical measurements. John Wiley & Sons, (2015).

[48] Florschuetz, L., Metzger, D., and Su, C., Heat transfer characteristics for jet array impingement with initial crossflow. In ASME 1983 International Gas Turbine Conference and Exhibit, American Society of Mechanical Engineers, pp. V004T09A001–V004T09A001, (1983).